GRB Afterglow of the Sub-relativistic Materials with Energy Injection

N. Fraija[1] , B. Betancourt Kamenetskaia[1,2,3] , A. Galvan-Gamez[1] , M. G. Dainotti[4,5] , R. L. Becerra[6] , S. Dichiara[7,8] ,
P. Veres[9] , and A. C. Caligula do E. S. Pedreira[1]

[1] Instituto de Astronomía, Universidad Nacional Autónoma de México, Circuito Exterior, C.U., A. Postal 70-264, 04510 México City, México
nifraija@astro.unam.mx
[2] TUM Physics Department, Technical University of Munich, James-Franck-Strasse, D-85748 Garching, Germany
[3] Max-Planck-Institut für Physik (Werner-Heisenberg-Institut), Föhringer Ring 6, 80805 Munich, Germany
[4] National Astronomical Observatory of Japan, Division of Science, Mitaka, 2-chome, Japan
[5] Space Science Institute, Boulder, CO, USA
[6] Instituto de Ciencias Nucleares, Universidad Nacional Autónoma de México, Apartado Postal 70-264, 04510 México, CDMX, Mexico
[7] Department of Astronomy, University of Maryland, College Park, MD 20742-4111, USA
[8] Astrophysics Science Division, NASA Goddard Space Flight Center, 8800 Greenbelt Road, Greenbelt, MD 20771, USA
[9] Center for Space Plasma and Aeronomic Research (CSPAR), University of Alabama in Huntsville, Huntsville, AL 35899, USA
Received 2022 January 18; revised 2022 April 24; accepted 2022 May 17; published 2022 July 19

Abstract

Sub-relativistic materials launched during the merger of binary compact objects and the core collapse of massive stars acquire velocity structures when expanding in a stratified environment. The remnant (either a spinning magnetized neutron star (NS) or a central black hole) from the compact object or core collapse could additionally inject energy into the afterglow via spin-down luminosity or/and by accreting fallback material, producing a refreshed shock, modifying the dynamics, and leading to rich radiation signatures at distinct timescales and energy bands with contrasting intensities. We derive the synchrotron light curves evolving in a stratified environment when a power-law velocity distribution parameterizes the energy of the shock, and the remnant continuously injects energy into the blast wave. As the most relevant case, we describe the latest multiwavelength afterglow observations ($\gtrsim 900$ days) of the GW170817/GRB 170817A event via a synchrotron afterglow model with energy injection of a sub-relativistic material. The features of the remnant and the synchrotron emission of the sub-relativistic material are consistent with a spinning magnetized NS and the faster *blue* kilonova afterglow, respectively. Using the multiband observations of some short bursts with evidence of kilonovae, we provide constraints on the expected afterglow emission.

Unified Astronomy Thesaurus concepts: Gamma-ray bursts (629); Non-thermal radiation sources (1119)

1. Introduction

Gamma-ray bursts (GRBs) are among the most powerful gamma-ray sources in the universe. They could be generated from the merger of binary compact objects (BCOs; Duncan & Thompson 1992; Usov 1992; Thompson 1994; Metzger et al. 2011) or the death of massive stars (Woosley 1993; Paczyński 1998; Woosley & Bloom 2006a). The merger of BCOs; a black hole (BH)–a neutron star (NS) or NS–NS, leading to kilonovae (KNe), is correlated with short-duration gamma-ray bursts (sGRBs; T_{90}[10] $\lesssim 2$ s; Li & Paczyński 1998; Rosswog 2005; Metzger et al. 2010; Kasen et al. 2013; Metzger 2017). On the other hand, long-duration gamma-ray bursts (lGRBs; $T_{90} \gtrsim 2$ s; Kouveliotou et al. 1993) are associated with the core collapse (CC) of dying massive stars (Woosley 1993; Galama et al. 1998) leading to supernovae (SNe; Bloom et al. 1999; Woosley & Bloom 2006b). It is believed that in both scenarios large quantities of materials with a wide range of velocities are ejected. In the framework of CC-SNe (depending on the type of SN association), several materials ejected with sub-relativistic

velocities less than $\beta \lesssim 0.4$[11] have been reported (see, e.g., Kulkarni et al. 1998; Bloom et al. 1999; Woosley & Bloom 2006b; Valenti et al. 2008; Gal-Yam 2017; Izzo et al. 2019, 2020; Modjaz et al. 2020; Nicholl et al. 2020). Regarding the merger of two NSs, sub-relativistic materials such as the cocoon, the shock breakout, and the dynamical and wind ejecta are launched with velocities in the range $0.03 \lesssim \beta \lesssim 0.8$[12] (see, e.g., Dessart et al. 2009; Metzger & Fernández 2014; Fernández et al. 2015; Kyutoku et al. 2014; Metzger et al. 2015; Nagakura et al. 2014; Murguia-Berthier et al. 2014; Lazzati et al. 2017, 2018; Goriely et al. 2011; Hotokezaka et al. 2013; Bauswein et al. 2013; Wanajo et al. 2014). While the mass and velocity inferred for the first GRB/KN association[13] were $M_{ej} \approx (10^{-4}-10^{-2})M_\odot$ and $\beta \approx (0.1-0.3)$, respectively (Coulter et al. 2017; Arcavi et al. 2017; Cowperthwaite et al. 2017; Nicholl et al. 2017; Metzger 2019), the mass and velocity inferred for the first GRB/SN association[14] was $M_{ej} \approx 10^{-5} M_\odot$ and $\beta \approx (0.2-0.3)$, respectively (Kulkarni et al. 1998).

In the sub-relativistic regime, the interaction of the decelerated material with the surrounding circumburst medium has been explored to interpret the multiwavelength observations in timescales from days to several years as synchrotron

---

[10] T_{90} is defined as the time during which the cumulative number of collected counts above background rises from 5% to 95%.

[11] Hereafter, we adopt natural units $c = \hbar = 1$.
[12] Some authors have considered the shock breakout material in the sub-, trans-, and ultra-relativistic regimes (see, e.g., Kyutoku et al. 2014; Metzger et al. 2015; Fraija et al. 2019c).
[13] GRB 170817A/AT 2017gfo.
[14] GRB 980425/SN1998bw.

afterglow models (see, e.g., Wijers et al. 1997; Dai & Lu 1999; Huang et al. 1999; Livio & Waxman 2000; Huang & Cheng 2003; Sironi & Giannios 2013; Barniol Duran & Giannios 2015). In most of the cases, the isotropic-equivalent kinetic energy of the materials launched during the coalescence of BCOs and the CC-SNe has been described by a power-law (PL) velocity distribution (see, e.g., Tan et al. 2001, and references therein).

The canonical X-ray light curve exhibits a typical shape that consists of four distinct PL segments $\propto t^{-\alpha}$ with a great flare (see, e.g., Zhang et al. 2006; Nousek et al. 2006). The initial steep decay with a temporal decay index $3 \lesssim \alpha \lesssim 5$, the normal decay phase with $0.9 \lesssim \alpha \lesssim 1.5$ and the late abrupt decay with $1.9 \lesssim \alpha \lesssim 2.4$ have been explained in terms of the end of the main episode, the standard synchrotron forward-shock model (Sari et al. 1998), and the post-jet-break decay phase (Vaughan et al. 2006), respectively. There is, however, one segment that occurs between the end of the prompt phase and the normal decay, a shallower than usual decay with $-0.1 \lesssim \alpha \lesssim 0.7$. This so-called *plateau* phase has been explained in several scenarios such as continuous energy injection from the central engine (either a spinning magnetized NS or a central BH) into the blast wave (Barthelmy et al. 2005; King et al. 2005; Dai et al. 2006; Perna et al. 2006; Proga & Zhang 2006; Burrows et al. 2005; Chincarini et al. 2007; Dall'Osso et al. 2017; Becerra et al. 2019a, 2019b), stratified ejecta (Toma et al. 2006; Jin et al. 2007; Hascoët et al. 2017), ejecta with a wide range of Lorentz factors (Rees & Mészáros 1998; Kumar & Piran 2000; Sari & Mészáros 2000; Zhang & Mészáros 2002; Fraija et al. 2019c), and variation of microphysical parameters (Fan & Piran 2006; Ioka et al. 2006; Fraija et al. 2020). Several modeling efforts of multiwavelength afterglows evoking energy injection by the central engine have been widely explored (see, e.g., Laskar et al. 2015; Zhao et al. 2021; Becerra et al. 2019a; Pereyra et al. 2022; Fraija et al. 2021b). For instance, Laskar et al. (2015) described GRB 100418A, GRB 100901A, GRB 120326A, and GRB 120404A and found that the majority of the kinetic energy of the relativistic jet in each burst was carried by slow-moving ejecta, thus indicating a correlation between the injection rates and the Lorentz factor distribution.

On 2017 August 17, a gravitational wave (GW) event (GW170817; Abbott et al. 2017a, 2017b) was linked with a faint gamma-ray prompt emission of GRB 170817A (Goldstein et al. 2017; Savchenko et al. 2017). Immediately, GRB 170817A was followed by an extensive observational campaign covering radio, optical, and X-ray bands (see, e.g., Troja et al. 2017; Abbott et al. 2017b; Kisaka et al. 2018; D'Avanzo et al. 2018a, and references therein). The observations of the nonthermal spectrum of GRB 170817A gathered during the first ≈ 900 days after the initial merger were analyzed by several authors. It was shown that they were consistent with synchrotron forward-shock emission generated by the deceleration of an off-axis structured jet with an opening angle $\theta_j \approx 5°$ that was observed from a viewing angle in the range of $15° \leqslant \theta_{obs} \leqslant 25°$ (Troja et al. 2017; Kasliwal et al. 2017b; Lamb & Kobayashi 2017, 2018; Resmi et al. 2018; Margutti et al. 2017a; Lazzati et al. 2017; Gottlieb et al. 2018b; Fraija et al. 2019b; Gottlieb et al. 2018b; Hotokezaka et al. 2018; Fraija et al. 2019c). In some proposed models, the off-axis structured jet is formed with an off-axis jet with a cocoon (Lazzati et al. 2017; Gottlieb et al. 2018b; Fraija et al. 2019b) and a shock breakout (Gottlieb et al. 2018b; Hotokezaka et al.

2018; Fraija et al. 2019c; Urrutia et al. 2021). Recently, Hajela et al. (2022) analyzed the latest X-ray and radio observations of GRB 170817A collected with the Chandra X-ray Observatory, the Very Large Array (VLA), and the MeerKAT radio interferometer about 3.3 yr after the initial merger. These new observations did not agree with the best-fit synchrotron curves from the off-axis jet model, thus reporting evidence of a new X-ray emission component. Given these contrasting observations, the authors offered the solution to explain this phenomenon in the context of either radiation from accretion processes on the compact-object remnant or a KN afterglow.

The study of properties of KNe has a great impact on the present-day field of study, especially given the link between GWs, sGRBs, and KN emission. The merger of two NSs associated with GW170817, GRB 170817A, and AT 2017gfo have provided the needed tools to predict the KN emission and its characteristics. While the prompt episode and the early afterglow are produced in internal and external shocks by an ultra-relativistic and extremely collimated jet, the KN transient is associated with a quasi-isotropic emission easier to detect at angles far away from those emitted from a collimated jet (Metzger & Berger 2012). Despite the advantageous prospects for detection, only four transient events with different brightness to AT 2017gf have been classified as KNe. They are associated with GRB 050709 (Jin et al. 2016), GRB 060614 (Yang et al. 2015), GRB 130603B (Tanvir et al. 2013; Berger et al. 2013), and GRB 160821B (Kasliwal et al. 2017a; Troja et al. 2019).

Recently, Fraija et al. (2021a) presented the afterglow light curves generated by the deceleration of sub-relativistic masses ejected from the merger of BCOs and the death of massive stars. The authors assumed that a PL velocity distribution describes the isotropic-equivalent kinetic energy of these masses and that the sub-relativistic ejected masses were decelerated, in turn, by a stratified-density environment. As a particular case, to explain the multiwavelength observations of the gravitational event GW170817/GRB 170817A at ~900 days, they constrained the parameter space of the synchrotron light curves of a sub-relativistic mass ejected during the merger of two NSs and decelerated in a constant-density environment. The synchrotron radiation of the sub-relativistic material was consistent with the faster *blue* KN afterglow. Inspired by the new observations of this GW event at 3.3 yr after the initial merger (Hajela et al. 2022), in this paper, we extend the synchrotron model presented in Fraija et al. (2021a), including the continuous energy injection from the central engine (either a spinning magnetized NS or BH remnant) into the blast wave through a numerical approach and analytic arguments. In addition, we apply the current model to potential candidates of sGRB events with evidence of a KN. The paper is organized as follows: Section 2 presents the dynamical evolution of the afterglow when the central engine continuously injects energy into the blast wave. We show an analytical solution and numerical approach. In Section 3, we show a synchrotron model with energy injection from a spinning magnetized NS and BH remnants. Section 4 shows the analysis of the multiwavelength light curves using typical values of the GRB afterglow. In Section 5, we apply our model to several potential candidates, including GW170817/GRB 170817A, and finally, in Section 6, we summarize. We consider the

convention $Q_x = \frac{Q}{10^x}$ in cgs units and assume for the cosmological constants a spatially flat universe Λ cold dark matter model with $H_0 = 69.6 \text{ km s}^{-1} \text{ Mpc}^{-1}$, $\Omega_M = 0.286$, and $\Omega_\Lambda = 0.714$ (Planck Collaboration et al. 2016).

2. Afterglow Light Curves with Energy Injection

2.1. Synchrotron Radiation

We consider electrons accelerated in the forward shock, which evolves in a stratified external environment with a density profile described by $\rho(r) = A_k\, r^{-k} = \frac{\dot{M}_W}{4\pi v_W} r^{-k}$, where $\dot{M}_W$ is the mass-loss rate and v_W is the wind velocity. There are two common choices of stratification, the value of $k = 0$ corresponds to the constant-density medium ($A_0 = n$), and $k = 2$ is associated with the density of the stellar wind ejected by its progenitor ($A_2 \simeq A_W\, 3 \times 10^{35} \text{ cm}^{-1}$) with A_W the density parameter. We assume that the shocked-accelerated electrons in the forward shocks can be described by a single PL energy distribution $\frac{dn}{d\gamma_e} \propto \gamma_e^{-p}$ for $\gamma_e \geqslant \gamma_m$ with p the spectral index and γ_m the Lorentz factor of the lowest-energy electrons.

The post-shock magnetic field evolves as $B' \propto A_k^{\frac{1}{2}} \beta^{\frac{2-k}{2}} t^{-\frac{k}{2}}$.[15] The Lorentz factors of the lowest-energy electrons and of the higher energy electrons, which are efficiently cooled by synchrotron emission evolve as $\gamma_m \propto \beta^2$ and $\gamma_c \propto A_k^{-1} \beta^{k-2} t^{k-1}$, respectively. It is worth noting that due to the synchrotron process, the effect that γ_c has on the electron energy distribution is to introduce a break. Given the evolution of the synchrotron frequency and the electron Lorentz factors, the corresponding spectral breaks can be written as $\nu_m \propto A_k^{\frac{1}{2}} \beta^{\frac{10-k}{2}} t^{-\frac{k}{2}}$ and $\nu_c \propto A_k^{-\frac{3}{2}} \beta^{\frac{3k-6}{2}} t^{\frac{3k-4}{2}}$. The terms ν_m and ν_c correspond to the characteristic and cooling spectral breaks, respectively. For $\nu_c < \nu_m$ the synchrotron spectrum lies in the fast-cooling regime and for $\nu_m < \nu_c$ this spectrum lies in the slow-cooling regime. In the self-absorption regime, the synchrotron spectral breaks evolve as $\nu_{a,1} \propto A_k^{\frac{4}{5}} \beta^{-\frac{4k+5}{5}} t^{\frac{3-4k}{5}}$ for $\nu_{a,1} \leqslant \nu_m \leqslant \nu_c$, $\nu_{a,2} \propto A_k^{\frac{p+6}{2(p+4)}} \beta^{\frac{10p-kp-6k}{2(p+4)}} t^{\frac{4-kp-6k}{2(p+4)}}$ for $\nu_m \leqslant \nu_{a,2} \leqslant \nu_c$, and $\nu_{a,3} \propto A_k^{\frac{9}{5}} \beta^{\frac{15-9k}{5}} t^{\frac{8-9k}{5}}$ for $\nu_{a,3} \leqslant \nu_c \leqslant \nu_m$. Taking into account that the peak spectral power evolves as $P_{\nu,\max} \propto A_k^{\frac{1}{2}} \beta^{\frac{2-k}{2}} t^{-\frac{k}{2}}$ and that the number of swept-up electrons in the post shock develop as $N_e \propto A_k \beta^{3-k} t^{3-k}$, the spectral peak flux density varies as $F_{\nu,\max} \propto A_k^{\frac{3}{2}} \beta^{\frac{8-3k}{2}} t^{\frac{3(2-k)}{2}}$ (details of the derivation are explicitly written in Fraija et al. 2021a).

Given the synchrotron spectral breaks and the maximum flux density, the synchrotron light curves in each cooling condition evolve as

$$F_\nu \propto \begin{cases} A_k^{-1}\beta^k t^{1+k}\, \nu^2, & \nu < \nu_{a,3}, \\ A_k^2 \beta^{5-2k} t^{\frac{11-6k}{3}} \nu^{\frac{1}{3}}, & \nu_{a,3} < \nu < \nu_c, \\ A_k^{\frac{3}{4}} \beta^{\frac{10-3k}{4}} t^{\frac{8-3k}{4}} \nu^{-\frac{1}{2}}, & \nu_c < \nu < \nu_m, \\ A_k^{\frac{p+2}{4}} \beta^{\frac{10p-k(p+2)}{4}} t^{\frac{8-k(p+2)}{4}} \nu^{-\frac{p}{2}}, & \nu_m < \nu, \end{cases} \tag{1}$$

$$F_\nu \propto \begin{cases} A_k^0 \beta^4 t^2\, \nu^2, & \nu < \nu_{a,1}, \\ A_k^{\frac{4}{3}} \beta^{\frac{7-4k}{3}} t^{\frac{9-4k}{3}} \nu^{\frac{1}{3}}, & \nu_{a,1} < \nu < \nu_m, \\ A_k^{\frac{p+5}{4}} \beta^{\frac{2(3+5p)-k(p+5)}{4}} t^{\frac{12-k(p+5)}{4}} \nu^{-\frac{p-1}{2}}, & \nu_m < \nu < \nu_c, \\ A_k^{\frac{p+2}{4}} \beta^{\frac{10p-k(p+2)}{4}} t^{\frac{8-k(p+2)}{4}} \nu^{-\frac{p}{2}}, & \nu_c < \nu, \end{cases} \tag{2}$$

and

$$F_\nu \propto \begin{cases} A_k^0 \beta^4 t^2\, \nu^2, & \nu < \nu_m, \\ A_k^{-\frac{1}{4}} \beta^{\frac{6+k}{4}} t^{\frac{8+k}{4}} \nu^{\frac{5}{2}}, & \nu_m < \nu < \nu_{a,2}, \\ A_k^{\frac{p+5}{4}} \beta^{\frac{2(3+5p)-k(p+5)}{4}} t^{\frac{12-k(p+5)}{4}} \nu^{-\frac{p-1}{2}}, & \nu_{a,2} < \nu < \nu_c, \\ A_k^{\frac{p+2}{4}} \beta^{\frac{10p-k(p+2)}{4}} t^{\frac{8-k(p+2)}{4}} \nu^{-\frac{p}{2}}, & \nu_c < \nu. \end{cases} \tag{3}$$

We want to emphasize that the synchrotron spectrum is always in the slow-cooling regime ($\nu_m < \nu_c$) and the spectrum in the fast-cooling regime ($\nu_c < \nu_m$) is derived for completeness since it is not relevant for the timescales investigated here. It is worth noting that the peak flux density is always at the peak of the spectrum.

The velocity β in the case of the coasting and deceleration phase without energy injection was derived in Fraija et al. (2021a). In the following, we derive the evolution of the velocity when the central engine continuously injects energy into the blast wave.

2.2. Dynamical Evolution

Energy injection by the central engine on the GRB afterglow can produce refreshed shocks. The luminosity injected from the central engine into the blast wave can be described by (e.g., Zhang et al. 2006)

$$\dot{E}_{\mathrm{inj}}(t) = L_{\mathrm{inj}}\left(\frac{t}{t_c}\right)^{-q}, \tag{4}$$

where q is the energy injection index, L_{inj} is the initial luminosity, and t_c is the characteristic timescale. The isotropic-equivalent kinetic energy can be estimated as

$$E_t = \int \dot{E}_{\mathrm{inj}}\, dt \propto L_{\mathrm{inj}}\, t^{-q+1}. \tag{5}$$

Given $q = 1$, the energy does not evolve with time and the standard synchrotron light curves are recovered (Sironi & Giannios 2013; Barniol Duran & Giannios 2015; Fraija et al. 2021a), and for $q > 1$, the decreasing value of isotropic-equivalent kinetic energy is not considered. The energy injection could be due to magnetic spin-down from a spinning magnetized NS ($q = 0$; Ruffert et al. 1997; Dai & Lu 1998, 2000; Zhang & Mészáros 2001) and a fallback material onto a central BH ($q \leqslant 1$) (Proga & Zhang 2006; Barthelmy et al. 2005; King et al. 2005; Dai et al. 2006; Perna et al. 2006; Proga & Zhang 2006; Burrows et al. 2005; Chincarini et al. 2007; Lei et al. 2013; Wu et al. 2013; Dall'Osso et al. 2017). It is relevant to mention that the spinning magnetized NS could also accrete material (see, e.g., Metzger et al. 2018). The luminosity due to magnetic spin-down (L_{sd}) or accreting BH (L_{BH}) scenario can be converted into flux through the efficiency in converting its spin-down/accreting energy to radiation (η) and the beaming factor of the wind ($f_b = 1 - \cos\theta_j$) with θ_j the half-opening angle. In both scenarios, the initial luminosity can be written as $L_{\mathrm{inj}} = \frac{\eta}{f_b} L_j$,

---

[15] Hereafter, we use prime and unprimed quantities for the comoving and observer frames, respectively.

and for typical and similar values of η and f_b, $L_{inj} \approx L_j$ with j = sd or BH.

During the deceleration phase, the ejected mass acquires a velocity structure, the velocity of matter in the front of the ejected mass is faster than the one that moves in the back (Sari & Mészáros 2000). Tan et al. (2001) studied the acceleration of the ejected mass with relativistic and sub-relativistic velocities. They found that the isotropic-equivalent kinetic energy in the sub- and ultra-relativistic limit can be expressed as a PL velocity distribution given by $E_k(\geqslant \beta) \propto \beta^{-5.2}$ for $\beta \ll 1$ and $E_k(\geqslant \beta\Gamma) \propto (\beta\Gamma)^{-1.1}$ for $\beta\Gamma \gg 1$ (with $\Gamma = \sqrt{1/1 - \beta^2}$), respectively.[16] Here, we consider the sub-relativistic regime, so the isotropic-equivalent kinetic energy distribution is given by

$$E_\beta(\geqslant \beta) = \tilde{E}\, \beta^{-\alpha}, \qquad (6)$$

where $\tilde{E}$ is the fiducial energy. We consider the PL velocity distribution in the sub-relativistic regime with the values of α in the range $3 \leqslant \alpha \leqslant 5.2$ presented in Tan et al. (2001). It is worth noting that these values of α in the sub-relativistic regime have been widely used (see, e.g., Hotokezaka & Piran 2015; Metzger 2017; Hajela et al. 2019).

The total isotropic-equivalent kinetic energy is given by the superposition of the energy injection (Equation (5)) and the energy distribution (Equation (6)). In the sub-relativistic regime, the ejected material is described by the Sedov–Taylor solution as

$$E_\beta + E_t = \left(\frac{5-k}{2}\right)^{3-k}\left(\frac{2\pi m_p}{3-k}\right)^{5-k}(1+z)^{k-3}A_k\beta^{5-k}t^{3-k}, \qquad (7)$$

where $E_\beta = \tilde{E}\beta^{-\alpha}$ and $E_t = \hat{E}\left(\frac{t}{t_c}\right)^{1-q}$ with $\hat{E} = \frac{1}{1-q}\, t_c\, L_{inj}$ for $q < 1$ and m_p the proton mass.

2.2.1. Analytical Solution

The Sedov–Taylor solution can be solved analytically in the asymptotic cases; $E_t \ll E_\beta$ and $E_\beta \ll E_t$. Each limiting case leads to a different velocity; they are given by

$$\beta \propto \begin{cases}(1+z)^{-\frac{k-3}{\alpha+5-k}} A_k^{-\frac{1}{\alpha+5-k}} \tilde{E}^{\frac{1}{\alpha+5-k}} t^{\frac{k-3}{\alpha+5-k}} & \text{for } E_t \ll E_\beta \\ (1+z)^{\frac{k-3}{k-5}} A_k^{\frac{1}{k-5}} \hat{E}^{-\frac{1}{k-5}} t^{\frac{q+2-k}{k-5}} & \text{for } E_\beta \ll E_t. \end{cases} \qquad (8)$$

Both cases may be written with just one expression:

$$\beta \propto (1+z)^{-\frac{k-3}{\alpha+5-k}} A_k^{-\frac{1}{\alpha+5-k}} E^{\frac{1}{\alpha+5-k}} t^{\frac{k-(q+2)}{\alpha+5-k}}, \qquad (9)$$

where the case $E_t \ll E_\beta$ is obtained by setting $q = 1$ with $E = \tilde{E}$, while the case $E_\beta \ll E_t$ is obtained by setting $\alpha = 0$ with $E = \hat{E}$. It is worth mentioning that the deceleration time can be obtained from Equation (9), and is presented in Appendix A.1. The blast-wave radius ($r = \beta t/(1 + z)$) can be written as

$$r \propto (1+z)^{-\frac{\alpha+2}{\alpha+5-k}} A_k^{-\frac{1}{\alpha+5-k}} E^{\frac{1}{\alpha+5-k}} t^{\frac{\alpha+3-q}{\alpha+5-k}}. \qquad (10)$$

The standard equations in constant-density medium are recovered when $q = 1$ and $\alpha = 0$ (i.e., $\beta \propto t^{-\frac{3}{5}}$ and $r \propto t^{\frac{2}{5}}$;

---

[16] The polytropic index $n_p = 3$ is used.

Sironi & Giannios 2013). The dynamics, spectral breaks, and synchrotron light curves derived in Fraija et al. (2021a) are recovered for $E_t \ll E_\beta$. Using Equations (9) and (10), we report in the Appendix the equations of the dynamics, the synchrotron spectral breaks, the flux density, and the light curves in the fast- and slow-cooling regime. It is worth noting that the synchrotron spectrum can lie in the slow- or fast-cooling regime, depending on the parameter values.

2.2.2. Numerical Approach: Comparison with Analytic Solution

We solve Equation (7) numerically using the bisection method[17] and plot the evolution of the shock's velocity for different parameter values, as shown in Figure 1. The rows represent different choices of luminosity, namely, the top one corresponds to a value of $L_{inj} = 10^{43}$ erg s^{-1} and the lower one to $L_{inj} = 10^{45}$ erg s^{-1}. The column on the left presents the velocity's development for different choices of the circumburst density profile $\propto r^{-k}$ with $k = 0$, 1, 1.5, 2, and 2.5. The center column displays its transformation according to different values of the isotropic-equivalent kinetic energy of the outermost matter's PL distribution index with $\alpha = 3.0$, 4.0, and 5.0. In the rightmost column, we show the evolution of the velocity for varying possibilities of the energy injection index, namely, $q = 0$, 0.5, and 1. For the panels in the middle and on the right-hand side, the solid lines represent a choice of constant-density medium ($k = 0$), while the dashed lines correspond to stellar wind ($k = 2$).

All panels show two distinct behaviors. At early times (before approximately 10 yr), the forward shock expands into the circumburst medium uninhibited with a constant velocity β_0, the so-called *coasting phase*, which is represented in the panels in Figure 1, as horizontal lines. Once the shock has interacted with enough material, the coasting phase comes to an end and the deceleration phase commences. It is governed by the solution of Equation (7) and can be seen in Figure 1 as the decrease in the velocity after its constant segment.

Upon comparison of the middle panels between both rows, it can be seen that when the dominant contribution to the energy of the shock is the fiducial energy $\tilde{E}$ (represented by the top row) the behavior of the shock's velocity depends more strongly on the velocity distribution's PL index α. This is made apparent from the separation of the curves for different values of this parameter in the deceleration phase, which is more pronounced in the top row for both constant density and wind-like environment.

On the other hand, the opposite behavior is noticed when the same comparison is performed between the rightmost panels. In this case, the energy injection parameter q's variation is more easily observed when $\hat{E}$ is the dominant component, as is made clear by the lower row in both types of medium considered. It is also apparent that when the energy that is injected into the shock is substantial, it may reach a quasi-constant value, where the energy injected equals the energy lost by interaction with the surrounding medium. This behavior is best exemplified by the dashed $q = 0$ curve in the lower panel, where it can be seen that the shock's velocity becomes quasi-constant even at late times.

---

[17] https://docs.scipy.org/doc/scipy/reference/generated/scipy.optimize.bisect.html
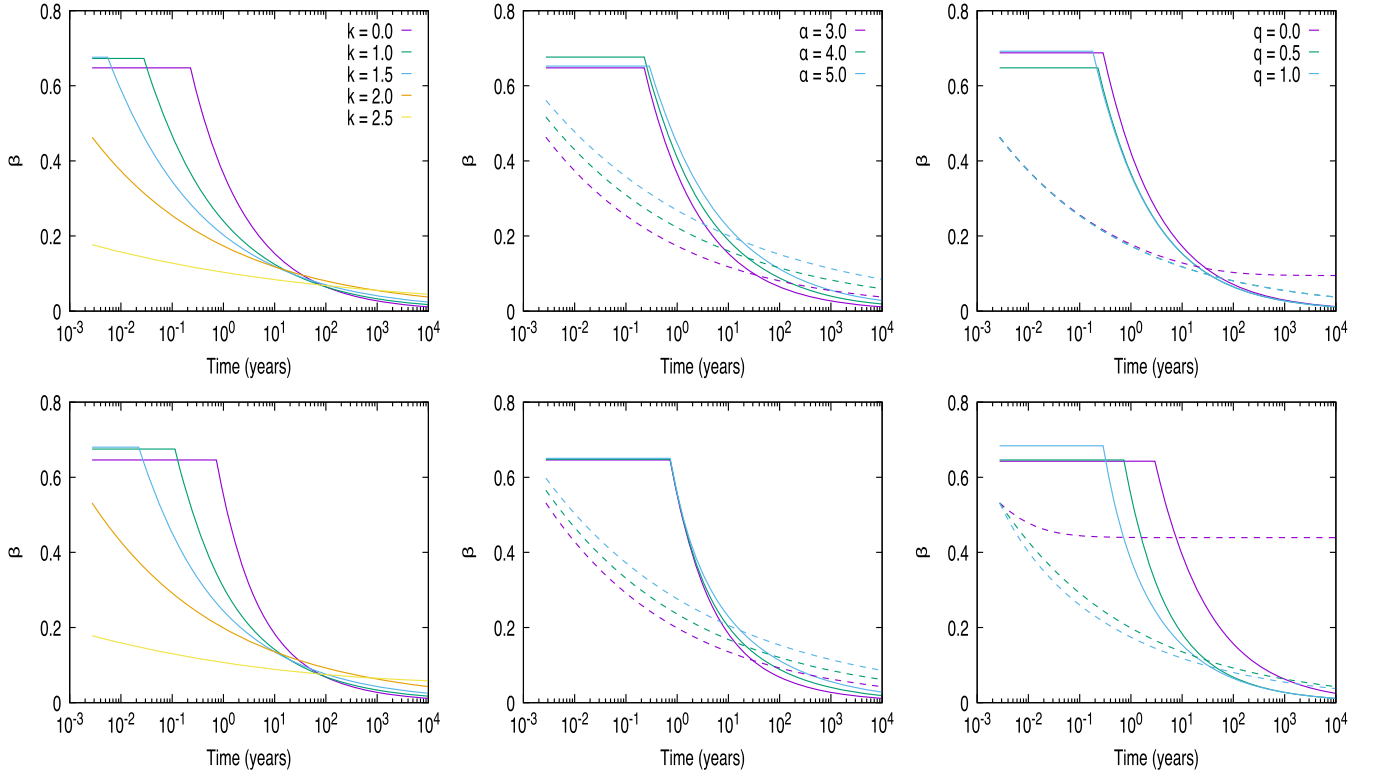
Figure 1. Evolution of the shock's velocity in time for different choices of parameters. The top row is equivalent to an energy injection luminosity of $L_{\rm inj} = 10^{43}$ erg s^{-1} and the lower one to $L_{\rm inj} = 10^{45}$ erg s^{-1}. Panels from left to right correspond to variation of the circumburst density distribution, the shock's velocity distribution, and the energy injection parameter, respectively. The solid lines in the middle and rightmost columns represent the case for a constant-density medium, while the dashed lines correspond to a wind-like one. The following parameters $\tilde{E} = 10^{49}$ erg and $z = 0.1$ are used.

3. Energy Injection from a Spinning Magnetized NS and an Accreting BH

A spinning magnetized NS and BH remnants are created from the merger of a BCO system (Price & Rosswog 2006; Siegel et al. 2013; Kiuchi et al. 2014) and the death of a massive star (Usov 1992; Dai & Lu 1998; Wheeler et al. 2000; Thompson et al. 2004; Bucciantini et al. 2007; Metzger et al. 2011). These remnants could accrete material and inject energy into the blast wave. The spinning magnetized NS or the central BH inject energy due to either a magnetic spin-down (Ruffert et al. 1997; Dai & Lu 1998, 2000; Zhang & Mészáros 2001) or accretion (Proga & Zhang 2006; Barthelmy et al. 2005; King et al. 2005; Dai et al. 2006; Perna et al. 2006; Proga & Zhang 2006; Burrows et al. 2005; Chincarini et al. 2007; Lei et al. 2013; Wu et al. 2013; Dall'Osso et al. 2017), respectively. For instance, Kasen et al. (2015) summarized a variety of final remnants from a merger of BCOs, which might inject energy into the blast wave; a hyper-massive NS that collapses into a BH in short timescales, a non-spinning BH, and a spinning magnetized NS and BH. In the case of a spinning magnetized NS or BH, the authors reported that the late-time activity via spin-down power or accreting material could be expected up to timescales of years. In this case, the synchrotron light curves from ejected materials would be modified by energy injection into the blast wave.

3.1. A Spinning Magnetized NS with Fallback Accretion

Rapid spinning magnetized NSs called *millisecond magnetars* are potential candidates for long and short GRBs. The

energy reservoir of a millisecond magnetar is the total rotation energy, which is given by

$$E = \frac{1}{2} I \, \Omega^2 \approx 2.6 \times 10^{52} \text{ erg } M_{\rm ns,1.4}^{\frac{3}{2}} \, P_{-3}^{-2}, \qquad (11)$$

where P is the spin period associated with an angular frequency $\Omega = 2\pi/P$ and $I \simeq 1.3 \times 10^{45} M_{\rm ns,1.4}^{\frac{3}{2}} \text{ g cm}^2$ (Lattimer & Schutz 2005) is the NS moment of inertia with $M_{\rm ns} = 1.4 \, M_\odot$ the NS mass. The merger of two NSs or CC-SN usually leaves a fraction of the stellar progenitor bound to the NS. This fraction of material will begin to rotate into an accretion disk and to fall back over a long period (Chevalier 1989; Rosswog 2007; Woosley & Heger 2012; Quataert & Kasen 2012). The fallback accretion rate can be written as (Metzger et al. 2018)

$$\dot{M} = \frac{2}{3} \frac{M_{\rm fb}}{t_{\rm fb}} \begin{cases} 1 & \text{for} \quad t < t_{\rm fb} \\ \left(\frac{t}{t_{\rm fb}}\right)^{-\frac{5}{3}} & \text{for } t_{\rm fb} < t, \end{cases} \qquad (12)$$

where $M_{\rm fb}$ is the accreting mass over a characteristic fallback time $t_{\rm fb}$. Once the millisecond magnetar is formed, the NS might be subject to fallback accretion. This accretion depends on the dipole magnetic moment (μ), and the Alfvén ($r_{\rm m}$), the corotation ($r_{\rm c}$) and cylinder ($r_{\rm lc}$) radii. The spin evolution of an accreting magnetar is given by Piro & Ott (2011),

$$I \frac{d\Omega}{dt} = -N_{\rm dip} + N_{\rm acc}, \qquad (13)$$

where the spin-down terms due to the torque and the accretion are

$$
N_{\text{dip}} \simeq \mu^2 \Omega^3 \begin{cases} \dfrac{r_{\text{lc}}^2}{r_{\text{m}}^2} & r_{\text{m}} \lesssim r_{\text{lc}}, \\ 1 & r_{\text{lc}} \lesssim r_{\text{m}}, \end{cases} \tag{14}
$$

and

$$
N_{\text{acc}} = \dot{M} (G_N \, M_{\text{ns}} \, r_{\text{m}})^{\frac{1}{2}} \left[1 - \left(\frac{r_{\text{m}}}{r_{\text{c}}} \right)^{\frac{3}{2}} \right], \tag{15}
$$

respectively, with G_N the gravitational constant, $\mu = BR_{\text{ns}}^3$ where $R_{\text{ns}} = 1.2 \times 10^6$ cm is the NS radius and B is the strength of the dipole magnetic field. For details, see Metzger et al. (2018). In this scenario, the isotropic-equivalent kinetic energy due to injection would be $E_t = \int L_{\text{inj}} \, dt = \frac{\eta}{f_b} \int L_{\text{sd}} \, dt$.

The panels on the left-hand side of Figure 2 show the spin-down luminosity and the synchrotron forward-shock light curves from the millisecond magnetar with an initial spin period $P_0 = 10^{-3}$ s (Metzger et al. 2018), an accreting mass $M_{\text{fb}} = 0.8 M_\odot$ (Metzger et al. 2018), a half-opening angle $\theta_j = 30°$ (Dhawan et al. 2020), and an efficiency $\eta = 0.1$ (Xiao & Dai 2019). The spin-down luminosities exhibit a plateau phase for an energy injection index of $q = 0$ (as indicated), and different timescales are observed for four different sets of parameters. The black solid curve corresponds to a magnetic field strength of $B = 10^{14}$ G and a characteristic fallback time of $t_{\text{fb}} = 10^3$ s (Metzger et al. 2018), the gray solid line takes the values $B = 10^{16}$ G and $t_{\text{fb}} = 10^3$ s, the black dashed one takes $B = 10^{14}$ G and $t_{\text{fb}} = 10^7$ s, and the gray dashed curve represents $B = 10^{16}$ G and $t_{\text{fb}} = 10^7$ s. It is worth noting that the gray dashed curve displays a spin-down luminosity $\approx 10^{42}$ erg s^{-1} during the plateau phase. Light curves show one or two plateau phases, depending on the values of the magnetic field, spin period, and the characteristic timescale of fallback. The first plateau related to a precursor is ~two orders of magnitude less than the second one, which is associated with the prompt emission. For small values of the characteristic timescale of fallback and larger values of magnetic field, the light curves exhibit a plateau in a timescale of seconds. Larger values of the characteristic timescale and small magnetic fields lead to a small luminosity during the plateau phase. The first plateau is explained when the Alfvén radius is larger than the corotation one ($r_c \ll r_m$). In this case, the spin-down luminosity becomes

$$
L_{\text{sd}} \simeq \left(\frac{\mu^2}{c \, r_{\text{m}}^2} + \dot{M} \, r_{\text{m}}^2 \right) \Omega_0 \exp\left(-\frac{t}{t_{\text{sd}}} \right), \tag{16}
$$

with $t_{\text{sd}} = \frac{1}{2} \left(\frac{\mu^2}{c^3 I r_{\text{m}}^2} + \frac{\dot{M} r_{\text{m}}^2}{I} \right)^{-1}$. For a large value of t_{sd} the spin-down luminosity decays very slowly. The second plateau can be explained once the equilibrium is reached and an analytic solution of Equation (13) can be derived (see Metzger et al. 2018; Fraija et al. 2021b). In this case, the spin-down luminosity becomes

$$
L_{\text{sd}} \approx 10^{40.7} \text{ erg s}^{-1} B_{16}^{-\frac{6}{7}} M_{\text{ns},1.4}^{\frac{12}{7}} R_{\text{ns},6.1}^{-\frac{18}{7}} \begin{cases} t^0 & \text{for } tv \ll t_{\text{fb}}, \\ t_8^{-\frac{50}{21}} & \text{for } t \gg t_{\text{fb}}, \end{cases} \tag{17}
$$

where the typical values of the accreting mass $M_{\text{fb}} = 0.8 M_\odot$ and the characteristic fallback time $t_{\text{fb}} = 10^8$ s are used. The profile of the spin-down luminosity (Equation (17)) agrees with the profiles shown in the panel on the upper left-hand side of Figure 2.

The black solid curve displays an uninterrupted drop during 10^3 days. The gray solid line presents a very similar behavior to its black counterpart as it decays with no interruption with the same PL. The main difference between both curves being that the luminosity achieved by this solution is smaller by about two orders of magnitude. The black dashed curve shows an initial plateau phase for approximately 10^{-1} days. Afterward, it decreases by about two orders of magnitude until it reaches its second plateau phase after a couple of days. This phase happens for roughly 1 month after which the luminosity drops once again with a PL slightly less steep than the one present in the previously mentioned solid curves. Finally, the gray dashed profile presents the same type of behavior as its black analog; however, this solution starts with larger values than the black line at early times and then drops below them during the black curve's first plateau phase. Afterward, the gray profile remains below the black one.

The panel in the lower left-hand side shows the light curves in this same scenario in three energy bands: radio (3 GHz), optical (R band), and X-ray (1 keV). All curves assume evolution in a constant-density medium $k = 0$ with $n = 5.88 \times 10^{-3}$ cm^{-3}, $\tilde{E} = 10^{48}$ erg, $z = 0.023$, $p = 2.15$, $\epsilon_B = 10^{-3}$, $\epsilon_e = 10^{-1}$, $\alpha = 3.0$, and $\beta = 0.3$ (Metzger 2017; Hajela et al. 2019; Fraija et al. 2021a; Hajela et al. 2022). The values of the magnetic field strength and characteristic timescale were chosen to be the same as the ones of the gray dashed line from the upper panel.

All three light curves grow with the same PL during the first 10^4 days. After this point in time, only the X-ray profile reaches its maximum and starts to drop, while the other two continue to rise, albeit with a smaller slope. The panel shows that the flux density of a profile increases with the energy of the band, that is, that the X-ray curve has the largest flux density, while the radio one has the smallest value.

3.2. Fallback Material onto a BH

The Eddington luminosity for pure ionized heavy elements is

$$
L_{\text{Edd}} = \frac{4\pi G_N M_{\text{BH}} m_p}{\sigma_T} = 10^{38.9} \text{ erg s}^{-1}, \tag{18}
$$

where $M_{\text{BH}} = 2.3 \, M_\odot$ is the mass of the remnant BH, σ_T is the Thompson cross section, and $Y_e \approx 0.4$.

The fallback material onto the remnant BH could create an accretion disk, powering a new material via Blandford–Znajek (BZ; Blandford & Znajek 1977), or neutrino-annihilation mechanism (Popham et al. 1999). The BZ jet power from a BH with mass M_{BH} and angular momentum J_{BH} can be
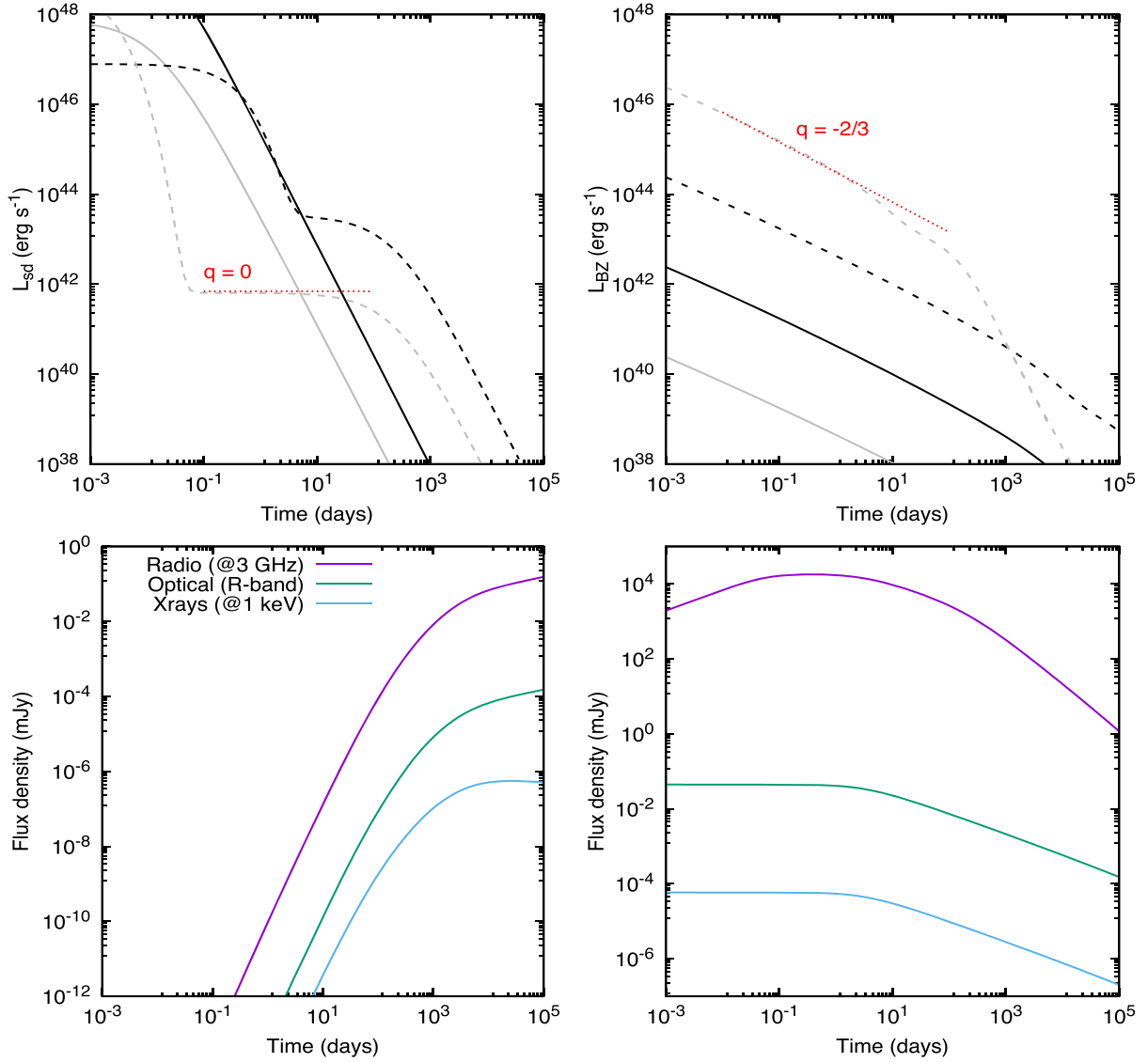
Figure 2. The spin-down and BZ luminosities (panels above) together with synchrotron forward-shock light curves (panels below) from a millisecond magnetar (left) and BH (right) with accretion. The spin-down luminosities are shown for $P_0 = 10^{-3}$ s and the parameters $B = 10^{14}$ G and $t_{\rm fb} = 10^3$ s (black solid line), 10^{16} G and 10^3 s (gray solid line), 10^{14} G and 10^7 s (black dashed line), and 10^{16} G and 10^7 s (gray dashed line). The BZ luminosities are shown for $t_0 = 0$ s, $t_p = 10^3$ s, $M_{\rm BH} = 2.3\, M_\odot$, and $a = 0.7$, and the parameters $\tau_{\rm vis} = 10^9$ s and $\dot{M}_p = 10^{-6}\, M_\odot$ s^{-1} (black solid line), 10^6 s and $10^{-5}\, M_\odot$ s^{-1} (gray solid line) 10^9 s and $10^{-4}\, M_\odot$ s^{-1} (black dashed line), and 10^{12} s and $10^{-5}\, M_\odot$ s^{-1} (gray dashed line). The synchrotron forward-shock light curves are shown in the radio (3 GHz), optical (R band), and X-ray (1 keV) bands with $\tilde{E} = 10^{48}$ erg, $p = 2.15$, $\epsilon_B = 10^{-3}$, $\epsilon_e = 10^{-1}$, $\alpha = 3.0$, and $\beta = 0.3$, and the parameters of the magnetar ($B = 10^{16}$ G and $t_{\rm fb} = 10^7$ s) and the BH ($t_0 = 0$ s, $t_p = 10^3$ s, $M_{\rm BH} = 2.3\, M_\odot$, $a = 0.7$, $\tau_{\rm vis} = 10^9$ s, and $\dot{M}_p = 10^{-6}\, M_\odot$ s^{-1}) model. We consider that the synchrotron light curves evolve in a constant-density medium with $k = 0$ and $n = 5.88 \times 10^{-3}$ cm^{-3} (left) and in a stellar-wind medium with $k = 2$ and $A_{\rm W} = 10^{-2}$ (right).

described as (Lee et al. 2000)

$$L_{\rm BZ} \approx 10^{49} {\rm erg\ s}^{-1}\, G(a)\dot{M}_{\rm BH,-5}, \qquad (19)$$

where $\dot{M}_{\rm BH,-5} = \frac{\dot{M}_{\rm BH}}{10^{-5}\, M_\odot\, {\rm s}^{-1}}$, $a = \frac{J_{\rm BH}}{G_N M_{\rm BH}^2}$ is the dimensionless spin parameter (see, e.g., Tchekhovskoy et al. 2008), $G(a) = \frac{a^2 F(a)}{(1 + \sqrt{1-a^2})^2}$ with $F(a) = [\frac{1+q'^2}{q'^2}][(q' + \frac{1}{q'})\arctan q' - 1]$ and $q' = \frac{a}{1 + \sqrt{1-a^2}}$ (Wu et al. 2013). The term $\dot{M}_{\rm BH}$ is the accretion rate onto the BH given by Kumar et al. (2008a, 2008b)

$$\dot{M}_{\rm BH} = \frac{1}{\tau_{\rm vis}} e^{-\frac{t}{\tau_{\rm vis}}} \int_{t_0}^{t} s\, e^{\frac{t'}{\tau_{\rm vis}}} \dot{M}_{\rm fb}\, dt', \qquad (20)$$

where $\tau_{\rm vis}$ is the viscous timescale, t_0 is the starting time of the accretion, and $\dot{M}_{\rm fb}$ is the accretion rate described by

Chevalier (1989); MacFadyen & Woosley (1999), MacFadyen et al. (2001), and Zhang et al. (2008).

$$\dot{M}_{\rm fb} = \frac{1}{2}\dot{M}_p \begin{cases} \left(\frac{t-t_0}{t_p - t_0}\right)^{\frac{1}{2}} & {\rm for}\ t < t_p \\ \left(\frac{t-t_0}{t_p - t_0}\right)^{-\frac{5}{3}} & {\rm for}\ t_p < t, \end{cases} \qquad (21)$$

with $\dot{M}_p$ and t_p the fallback rate and the time at the peak, respectively. For details, see Wu et al. (2013). In this scenario, the isotropic-equivalent kinetic energy due to injection would be $E_t = \frac{\eta}{f_b} \int L_{\rm BZ}\, dt$.

The panels on the right-hand side of Figure 2 are analogous to their counterparts on the left-hand side, which were explained in the previous subsection, but now in the context of the fallback

material onto a BH scenario. The upper panel presents the BZ luminosity with $q = 2/3$ (as indicated in the dashed gray line) with different timescales. This behavior corresponds to an accretion rate of $\dot{M}_{fb} \propto t^{\frac{1}{2}}$. The change in the slope in the BZ luminosity is associated with the variation of the accretion rate from $\dot{M}_{fb} \propto t^{\frac{1}{2}}$ to $\propto t^{-\frac{5}{3}}$ (see Equation (21)). It is worth noting that the BH torus system has no effect on the afterglow evolution at later times, which corresponds to an accretion rate of $\propto t^{-\frac{5}{3}}$ (e.g., MacFadyen et al. 2001; Janiuk et al. 2004; Zhang et al. 2006). We consider typical values of starting timescale of accretion $t_0 = 1$ s, timescale at the peak $t_p = 10^3$ s (Wu et al. 2013), BH mass $M_{BH} = 2.3\,M_\odot$, and dimensionless spin parameter $a = 0.7$ (Wu et al. 2013; Zhao et al. 2021). Once again, four different sets of parameters were considered. The black solid curve corresponds to a viscous timescale of $\tau_{vis} = 10^9$ s and a fallback rate of $\dot{M}_p = 10^{-6}\,M_\odot$ s^{-1} (Zhao et al. 2021), the gray solid line takes the values 10^6 s and $10^{-5}\,M_\odot$ s^{-1}, the black dashed one takes 10^9 s and $10^{-4}\,M_\odot$ s^{-1}, and the gray dashed curve represents 10^{12} s and $10^{-5}\,M_\odot$ s^{-1}. In a similar fashion to the panel on the left-hand side, both of the solid curves have similar behavior. They both decrease following the same PL and the black profile is greater than the gray one by about two orders of magnitude. In the case of the dashed lines, the black solution decreases uninterrupted, but it changes its PL at around 10^4 days. The gray curve also decreases with no interruption and follows the same slope as the black one at early times, but it changes its slope at approximately 10^2 days. It is also interesting to note, that similarly to the panel on the left-hand side, the gray dashed profile starts with a greater luminosity than its black counterpart, but it falls below it at later times, namely, in the vicinity of 10^3 days.

The lower panel on the right-hand side shows the synchrotron forward-shock light curves in this scenario in the same energy bands as in the panel to its left. The deceleration was once again assumed to be in a wind-like medium $k = 2$ with $A_W = 10^{-2}$ cm^{-3} and the values of the viscous timescale and fallback rate were chosen to be the same as the ones of the gray dashed line from the upper panel. The rest of the parameters were selected as $\tilde{E} = 10^{48}$ erg, $z = 0.023$, $p = 2.15$, $\epsilon_B = 10^{-3}$, $\epsilon_e = 10^{-1}$, $\alpha = 3.0$, and $\beta = 0.3$ (Metzger 2017; Hajela et al. 2019; Fraija et al. 2021a; Hajela et al. 2022). In all cases, the BZ luminosity is much higher than the Eddington luminosity.

The optical and X-ray bands have the exact same behavior, namely, that their light curve reaches its peak very early, it remains constant until ~ 10 days, and from this moment onward its flux density decreases. It is worth noting that both of these curves follow the same PLs; the difference between them being that the optical band lies two orders of magnitude above the X-ray band. The case of the radio light curve is different, as it can be observed that it reaches its maximum later than the previously mentioned profiles. Its constant phase also lasts less time and its behavior at late times is according to a PL with a steeper slope than the one of the other two energy bands.

Upon comparison of the two upper panels of Figure 2, it can be observed that, in general, the luminosities in the context of a BH decrease in time less steeply than the ones from a millisecond magnetar. It can also be noted that for a BH, there is no appearance of the so-called *plateau* phase, which is a characteristic that could discriminate between both scenarios.

In the case of the lower panels of the aforementioned figure, it can be concluded that the flux density increases in smaller timescales in the BH scenario, as in this case the maximum is

reached at $\sim 10^{-1}$ days, while in the case of the magnetar it is obtained at $\sim 10^3$ days. The same observation can be made for the drop in the flux; as can be seen from the figure, the light curves in the right panel begin to decrease at $\sim 10^1$ days, while in the left panel a drop is not apparent in any of the energy bands shown even at $\sim 10^5$ days.

An analytic solution of Equation 19 can be derived for $t_p < t$ ($\dot{M}_{fb} \propto t^{-\frac{5}{3}}$) with $t \ll \tau_{vis}$. In this case, the term $e^{\pm \frac{t'}{\tau_{vis}}} \approx 1$ and therefore the BZ luminosity becomes

$$L_{BZ} \approx 10^{49} \text{erg s}^{-1}\, \tau_{vis,7}^{-1}\, \dot{M}_{p,-6}\, t_7^{-\frac{2}{3}}, \tag{22}$$

with $\dot{M}_{p,-6} = \frac{\dot{M}_{BH}}{10^{-6}\,M_\odot\,s^{-1}}$. The profile of the BZ luminosity (Equation (22)) agrees with the profiles shown in the panel on the upper right-hand side of Figure 2.

It is worth mentioning that the neutrino-annihilation luminosity could not describe late-time activities (see, e.g., Zhao et al. 2021), and therefore, it cannot be considered in this work.

4. Analysis of the Multiwavelength Afterglow Light Curves

4.1. Synchrotron Emission

Some examples of the light curves in several energy bands are shown in Figures 3–7. Each figure, in ascending order, presents the radiative behavior produced by the interaction between the sub-relativistic ejecta and its surrounding medium, which is described by a density profile $A_k r^{-k}$ with $k = 0, 1, 1.5, 2,$ and 2.5, respectively. The panels from top to bottom correspond to the electromagnetic bands in radio at 1.6 GHz, optical at the R band, and X-rays at 1 keV for $\tilde{E} = 10^{49}$ erg, $\epsilon_B = 10^{-3}$, $\epsilon_e = 10^{-1}$, and $z = 0.023$ (Metzger 2017; Hajela et al. 2019; Fraija et al. 2021a; Hajela et al. 2022). The panels on the left-hand side show the light curves for $p = 2.6$ with $\alpha = 3.0, 4.0,$ and 5.0, and the panels on the right-hand side show the light curves for $\alpha = 3.0$ with $p = 2.2, 2.8,$ and 3.4.

We present the predicted synchrotron light curves in the previously mentioned energy bands for typical values of GRB afterglows. Most light curves peak on timescales from several months to a few years, which is in agreement with the observations of some SNe, such as SN 2014C (Margutti et al. 2017b) and SN2016aps (Nicholl et al. 2020). There is an outlier, however, present in the flux in the radio band for $p = 3.4$ and $\alpha = 3.0$, which reaches its maximum in a timescale of a couple of days for stratified media when $k > 1.5$. The synchrotron light curves are shown using a stratified medium with density profile $\propto r^{-k}$ with $k = 0, 1, 1.5, 2,$ and 2.5, which covers both long and short GRB progenitors. The constant-density medium ($k = 0$) is usually related to short GRBs, which stem from the merger of two NSs, while the stratified medium ($1 \leqslant k \leqslant 2.5$) is only associated with long GRBs from dying massive stars with different mass-loss evolution. For instance, Yi et al. (2013) investigated the evolution of the emission of forward-reverse shocks propagating in a medium described by the previously mentioned PL distributions. They applied their model to 19 GRBs and found that the density profile index took values of $0.4 \leqslant k \leqslant 1.4$, with a typical value of $k \sim 1$. This value was also obtained by Liang et al. (2013), who analyzed a bigger sample of 146 GRBs.

All figures show that during the early stages of the evolution there is an increase in the flux. During this epoch, when the sub-relativistic material decelerates in a constant-density
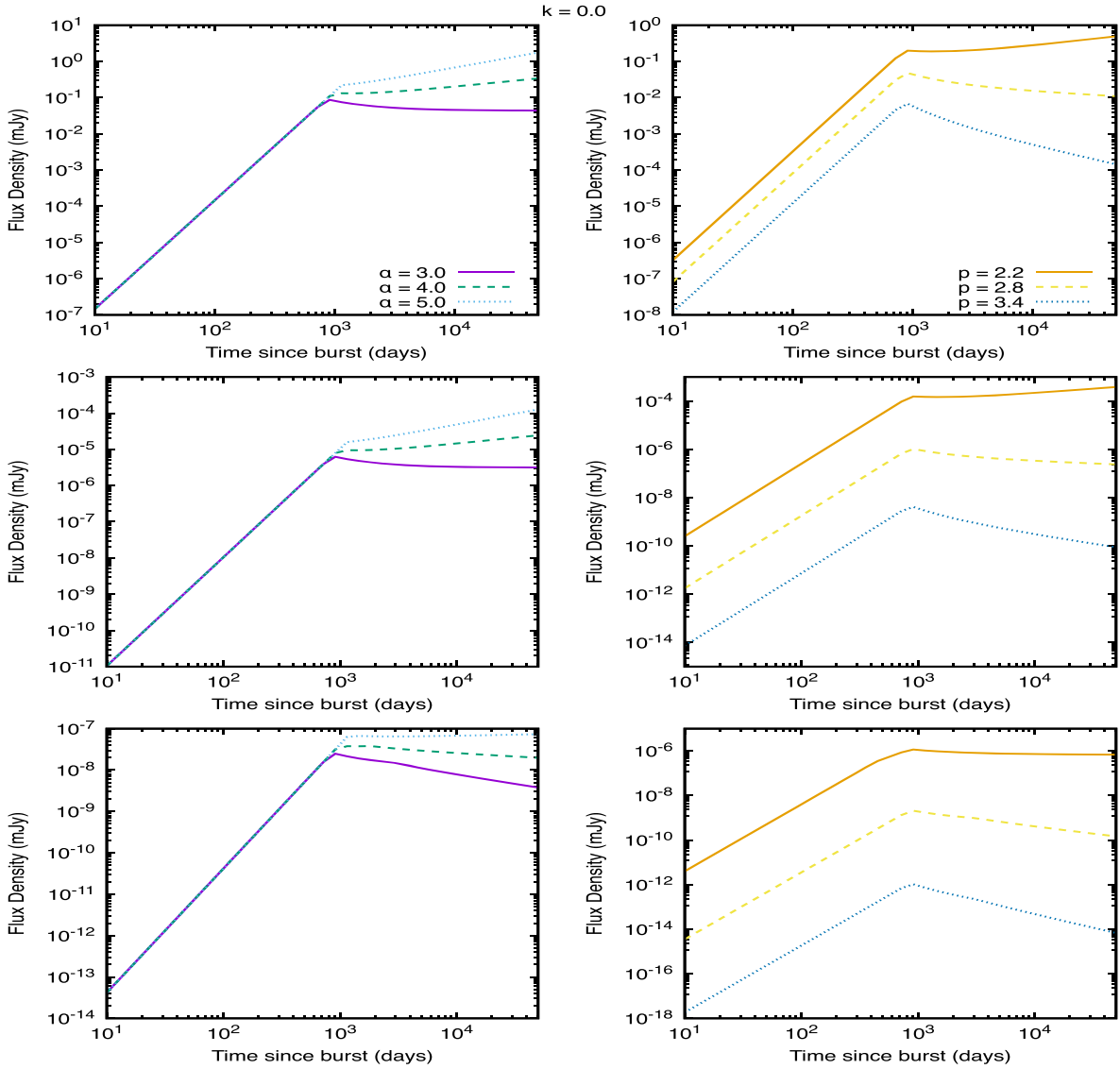
Figure 3. Synchrotron light curves generated by the deceleration of the sub-relativistic ejecta for $k = 0$. The panels from top to bottom correspond to the radio (1.6 GHz), optical (R band), and X-ray (1 keV) bands, respectively. The panels on the left-hand side show the light curves for $p = 2.6$ with $\alpha = 3$, 4, and 5, and the panels on the right-hand side show the light curves for $\alpha = 3$ with $p = 2.2$, 2.8, and 3.4. The following parameters $P_0 = 10^{-3}$ s, $B = 10^{14}$ G, $t_{fb} = 10^3$ s, $\tilde{E} = 10^{51}$ erg, $A_0 = 1$ cm^{-3}, $\epsilon_B = 10^{-4}$, $\epsilon_e = 10^{-1}$, and $d_z \approx 100$ Mpc ($z = 0.023$) are used.

medium, the light curve grows steeply. For more stratified media, this growth is not as evident, as the example presented in Figure 7, where the early-time behavior is more gradual. That is to say, the amount of time during which the flux grows depends on the stratification of the surrounding medium. This is exemplified by Figures 3 and 4, where the rise in the flux is evident, while in subsequent figures this growth is not observed, which means that this phase happens much quicker as the stratification is increased. This result implies that if such a flattening or rebrightening at timescales from months to years in the light curve was observed together with GW detection, then this would be associated with the deceleration of a sub-relativistic material launched during the merger of two NSs. Otherwise, we show that an observed flux that gradually decreases on timescales from months to years could be associated with the deceleration of a sub-relativistic material launched during the death of a massive star with different mass-loss evolution at the end of its life. It is worth noting that all these results are for on-axis observers, and for an off-axis

observer the flux would decrease as the viewing angle between the material and the observer increases. For a relativistic off-axis component in the outflow, the spectral breaks and the maximum flux are corrected by the Doppler factor (δ_D) as $\nu_i = \delta_D/(1 + z)\nu'_i$ with $i = a$, m, c, and $F_{\nu,\max} = \frac{(1+z)^2\delta_D^3}{4\pi d_z^2}N_e P'_{\nu'_m}$, respectively, where $P_{\nu_m} = \delta_D/(1 + z)P'_{\nu'_m}$ is the radiation power and $N_e = (\Omega/4\pi)n(r)\frac{4\pi}{3-k}r^3$ is the total number of emitting electrons with $r = \delta_D/(1 + z)\Gamma\beta ct$ the shock radius and the transformation law for the solid angle as $\Omega = \Omega'/\delta_D^2$. The Doppler factor is defined as $\delta_D = \frac{1}{\Gamma(1 - \mu\beta)}$ with $\mu = \cos\Delta\theta$, Γ the bulk Lorentz factor, and $\Delta\theta = \theta_{obs} - \theta_j$ given by the viewing angle (θ_{obs}) and the half-opening angle of the jet (θ_j).

Table 1 shows the evolution of the density parameter in each cooling condition of the synchrotron afterglow model. For instance, the synchrotron light curve in the slow-cooling regime as a function of the density parameter is given by F_ν: $\propto A_k^{\frac{4\alpha+13}{3(\alpha+5-k)}}$

Table 1
PL Indexes of the Density Parameter in Each Cooling Condition of the Synchrotron Afterglow Model

	$k=0$	$k=1$	$k=1.5$	$k=2$	$k=2.5$
$\nu_{a,3} \leqslant \nu_c \leqslant \nu_m$					
$\nu < \nu_{a,3}$	-1	$-\frac{\alpha+5}{\alpha+4}$	$-\frac{2(\alpha+5)}{2\alpha+7}$	$-\frac{\alpha+5}{\alpha+3}$	$-\frac{2(\alpha+5)}{2\alpha+5}$
$\nu_{a,3} < \nu < \nu_c$	$\frac{2\alpha+5}{\alpha+5}$	$\frac{2\alpha+5}{\alpha+4}$	$\frac{2(2\alpha+5)}{2\alpha+7}$	$\frac{2\alpha+5}{\alpha+3}$	2
$\nu_c < \nu < \nu_m$	$\frac{3\alpha+5}{4(\alpha+5)}$	$\frac{3\alpha+5}{4(\alpha+4)}$	$\frac{3\alpha+5}{2(2\alpha+7)}$	$\frac{3\alpha+5}{4(\alpha+3)}$	$\frac{3\alpha+5}{2(2\alpha+5)}$
$\nu_m < \nu$	$\frac{\alpha(p+2)-5(p-2)}{4(\alpha+5)}$	$\frac{p(\alpha-5)+2(\alpha+5)}{4(\alpha+4)}$	$\frac{p(\alpha-5)+2(\alpha+5)}{2(2\alpha+7)}$	$\frac{p(\alpha-5)+2(\alpha+5)}{4(\alpha+3)}$	$\frac{p(\alpha-5)+2(\alpha+5)}{2(2\alpha+5)}$
$\nu_{a,1} \leqslant \nu_m \leqslant \nu_c$					
$\nu < \nu_{a,1}$	$-\frac{4}{\alpha+5}$	$-\frac{4}{\alpha+4}$	$-\frac{8}{2\alpha+7}$	$-\frac{4}{\alpha+3}$	$-\frac{8}{2\alpha+5}$
$\nu_{a,1} < \nu < \nu_m$	$\frac{4\alpha+13}{3(\alpha+5)}$	$\frac{4\alpha+13}{3(\alpha+4)}$	$\frac{2(4\alpha+13)}{3(2\alpha+7)}$	$\frac{4\alpha+13}{3(\alpha+3)}$	$\frac{2(4\alpha+13)}{3(2\alpha+5)}$
$\nu_m < \nu < \nu_c$	$\frac{5\alpha+19+p(\alpha-5)}{4(\alpha+5)}$	$\frac{5\alpha+19+p(\alpha-5)}{4(\alpha+4)}$	$\frac{5\alpha+19+p(\alpha-5)}{2(2\alpha+7)}$	$\frac{5\alpha+19+p(\alpha-5)}{4(\alpha+3)}$	$\frac{5\alpha+19+p(\alpha-5)}{2(2\alpha+5)}$
$\nu_c < \nu$	$\frac{\alpha(p+2)-5(p-2)}{4(\alpha+5)}$	$\frac{p(\alpha-5)+2(\alpha+5)}{4(\alpha+4)}$	$\frac{5(2-p)+\alpha(p+2)}{2(2\alpha+7)}$	$\frac{p(\alpha-5)+2(\alpha+5)}{4(\alpha+3)}$	$\frac{p(\alpha-5)+2(\alpha+5)}{2(2\alpha+5)}$
$\nu_m \leqslant \nu_{a,2} \leqslant \nu_c$					
$\nu < \nu_m$	$-\frac{4}{\alpha+5}$	$-\frac{4}{\alpha+4}$	$-\frac{8}{2\alpha+7}$	$-\frac{4}{\alpha+3}$	$-\frac{8}{2\alpha+5}$
$\nu_m < \nu < \nu_{a,2}$	$-\frac{\alpha+11}{4(\alpha+5)}$	$-\frac{\alpha+11}{4(\alpha+4)}$	$-\frac{\alpha+11}{2(2\alpha+7)}$	$-\frac{\alpha+11}{4(\alpha+3)}$	$-\frac{\alpha+11}{2(2\alpha+5)}$
$\nu_{a,2} < \nu < \nu_c$	$\frac{19+p(\alpha-5)+5\alpha}{4(\alpha+5)}$	$\frac{19+p(\alpha-5)+5\alpha}{4(\alpha+4)}$	$\frac{19+p(\alpha-5)+5\alpha}{2(2\alpha+7)}$	$\frac{19+p(\alpha-5)+5\alpha}{4(\alpha+3)}$	$\frac{19+p(\alpha-5)+5\alpha}{2(2\alpha+5)}$
$\nu_c < \nu$	$\frac{\alpha(p+2)-5(p-2)}{4(\alpha+5)}$	$\frac{p(\alpha-5)+2(\alpha+5)}{4(\alpha+4)}$	$\frac{p(\alpha-5)+2(\alpha+5)}{2(2\alpha+7)}$	$\frac{p(\alpha-5)+2(\alpha+5)}{4(\alpha+3)}$	$\frac{p(\alpha-5)+2(\alpha+5)}{2(2\alpha+5)}$

for $\nu_{a,1} < \nu < \nu_m$, $\propto A_k^{\frac{5\alpha+19+p(\alpha-5)}{4(\alpha+5-k)}}$ for $\nu_m < \nu < \nu_c$ and $A_k^{\frac{p(\alpha-5)+2(\alpha+5)}{4(\alpha+5-k)}}$ for $\nu_c < \nu$. Any variation of the density will be better observed in low-energy frequencies, such as radio. Additionally, it shows that variations of the density profile index are more apparent in the radio light curve when compared to the other fluxes in the other energy bands. This change in the density profile is also more easily appreciated for large values of α, namely, 4.0 and 5.0. Therefore, a transition between density profiles will be more easily observed in the radio band with high values of the velocity distribution parameter.

4.2. Comparison with and without Energy Injection

Figure 8 shows several synchrotron light curves in order to compare the effects of the continuous injection of energy into the blast wave. It is divided into two columns, the one on the left considers a constant-density medium ($k=0$) with the millisecond magnetar remnant, while the one on the right takes into account a stellar wind ($k=2$) with the scenario of fallback material onto a BH. The panels from top to bottom correspond to the radio (1.6 GHz), optical (R band), and X-ray (1 keV), respectively. Every panel shows two curves, the dashed line represents the evolution of the flux density with energy injection, and the solid line stands for an evolution with no injection of energy.

It can be seen in all panels on the left that regardless of injection of energy or not, both solutions are the same at early times. However, all solid curves remain several orders of magnitude below their dashed counterparts after the evolution has reached times of approximately 20 days. There also seems to be a difference in timescales when the maximum is reached, as the dashed curves reach it within the limits of the plot, while the solid lines continue their upward trend. This is noted by observing that for late times ($>10^4$ days) the rise in the light curve is steeper when there is energy injection, while the

solution represented by the dashed lines reaches its peak with a smaller slope and then begins to drop.

On the other hand, the panels on the right present contrasting behavior, as both the case with energy injection and the case without reach the same peak flux, the only difference between them being the decay of the light curves. For a stellar-wind environment, the late-time behavior is the opposite of the constant medium case, namely, the flux density drops and this decay is less sharp when there is energy injection.

Upon comparison between the columns on the right and left, it can also be observed that the early time behavior is different in the optical and X-ray bands. Regardless of whether there is energy injection or not, the flux density in the constant medium increases until its peak. For a stellar-wind environment, however, the light curve remains constant and begins to decay very slowly. This behavior is due to the change in the energy injection. At early times it evolves as $q = 2/3$ (up to 10^3 days), and at later times with $\dot{M}_{fb} \propto t^{-\frac{5}{3}}$ the BH torus system has no effect on the afterglow evolution (e.g., MacFadyen et al. 2001; Janiuk et al. 2004; Zhang et al. 2006). It is worth noting that after 10^3 days both curves decrease with a similar slope, as expected. We emphasize that for $q = 1$ the standard synchrotron light curves are recovered (e.g., Zhang et al. 2006).

5. Synchrotron Emission from Different Ejected Materials and Applications

It is believed that sub-energetic GRBs are quasi-spherical explosions whose dominating components are the sub-relativistic materials, which contribute approximately 99.9% of the explosion's energy. The mildly relativistic materials, on the other hand, correspond to only $\approx 0.1\%$ (see, e.g., Margutti et al. 2014; Modjaz et al. 2020). There is wide agreement in the community that the origin of sGRBs and lGRBs is closely related to the merger of BCOs and the death of massive stars leading to KNe
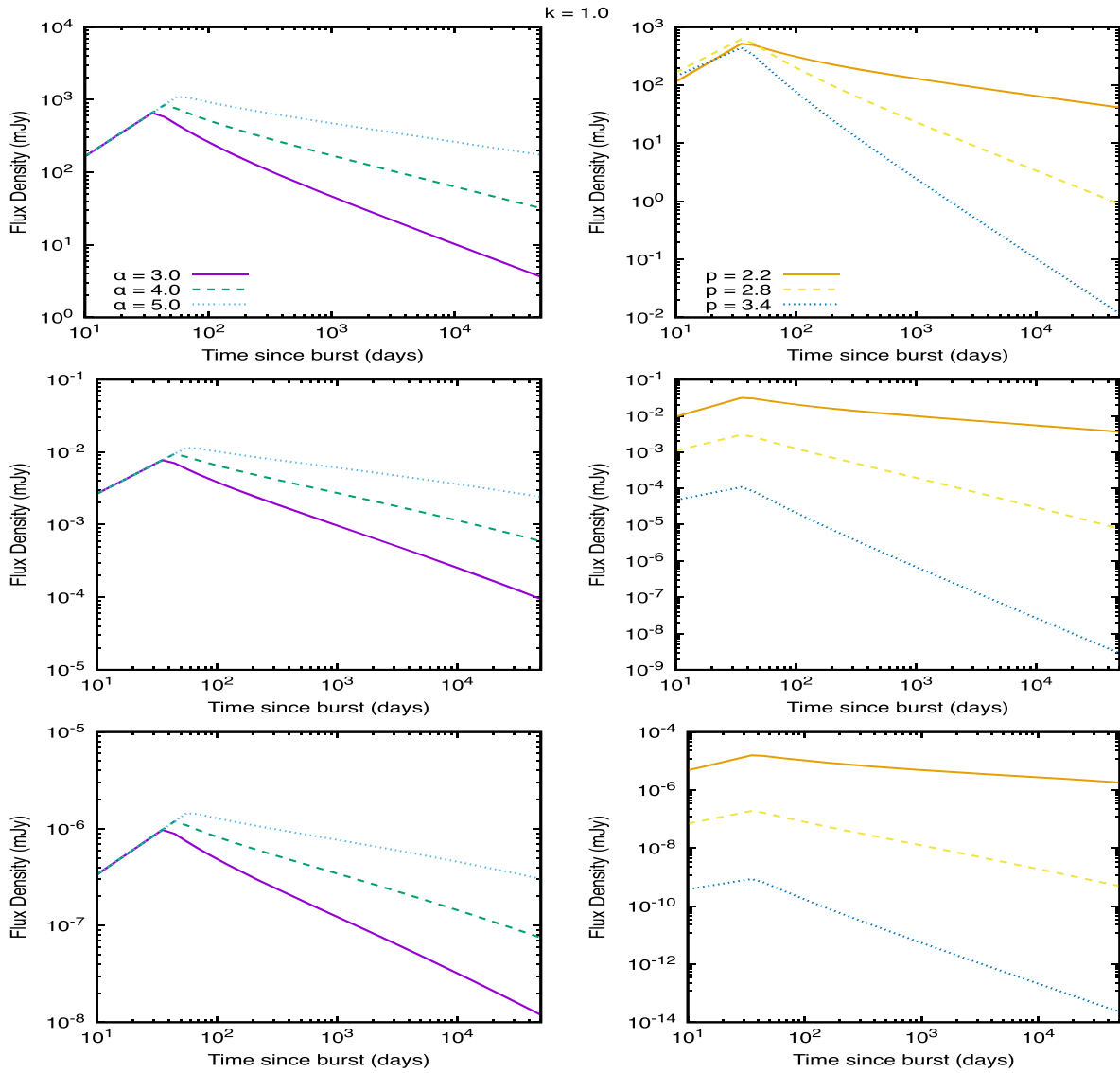
Figure 4. The same as Figure 3, but for $k = 1.0$ with $A_1 = 1.5 \times 10^{19}$ cm^{-2}.

and SNe, respectively. In addition to KN and SN materials, other types of materials are launched into the circumstellar medium with different velocities, and as such, will contribute at distinct timescales in distinct energy bands with contrasting intensities. In the following, we will present a brief introduction to the values of masses, the isotropic-equivalent kinetic energies, and velocities of each decelerated material that is ejected during the merger of two NSs, namely, the dynamical ejecta, the shock breakout material, the disk wind, and the cocoon material.

Dynamical ejecta—At the moment of the merger of two NSs, matter is ejected dynamically from their surfaces due to gravitational and hydrodynamical interactions (Davies et al. 1994; Ruffert et al. 1997; Rosswog et al. 1999). Based on numerical simulations, the mass of the material liberated, the kinetic energy, and the velocities lie in the ranges of $10^{-4} \lesssim M_{\rm ej} \lesssim 10^{-2} M_\odot$, $10^{49} \lesssim \tilde{E} \lesssim 10^{51}$ erg, and $0.1 \lesssim \beta\Gamma \lesssim 0.3$, respectively (see, e.g., Goriely et al. 2011; Hotokezaka et al. 2013; Bauswein et al. 2013; Piran et al. 2013; Wanajo et al. 2014; Grossman et al. 2014).

Shock breakout material—A shock at the interface between the two NSs is formed the moment directly after their

coalescence. This shock manages to break out from the NS core to the crust at sub-relativistic velocities ($\beta_{\rm in} \simeq 0.25$; see, e.g., Kyutoku et al. 2014; Metzger et al. 2015). When the shocked material reaches half of the escape velocity it converts a fraction of the shock-heated internal energy into kinetic energy and it escapes the merger into a nearly vacuum region (for details see Kyutoku et al. 2014; Fraija et al. 2019c). The shock breakout material's properties depend on the mass, radius, and velocity of the merger remnant. Numerical simulations indicate that the material mass, the kinetic energy, and the velocities lie in the ranges of $10^{-6} \lesssim M_{\rm ej} \lesssim 10^{-4} M_\odot$, $10^{47} \lesssim \tilde{E} \lesssim 10^{50.5}$ erg, and $\beta\Gamma \gtrsim 0.8$, respectively (see, e.g., Kyutoku et al. 2014; Metzger et al. 2015).

Disk wind—The coalescence of the NS binary will end in a tidal disruption and some of the material of the stars will be shed, forming an accretion disk around the central remnant. This component of the sub-relativistic material represents a significant portion of the total material mass and might dominate over other constituents (Siegel & Metzger 2017). The mass of the accretion disk will depend on the initial NS spins and is located in the range of $10^{-3} \lesssim M_{\rm ej} \lesssim 0.3 M_\odot$
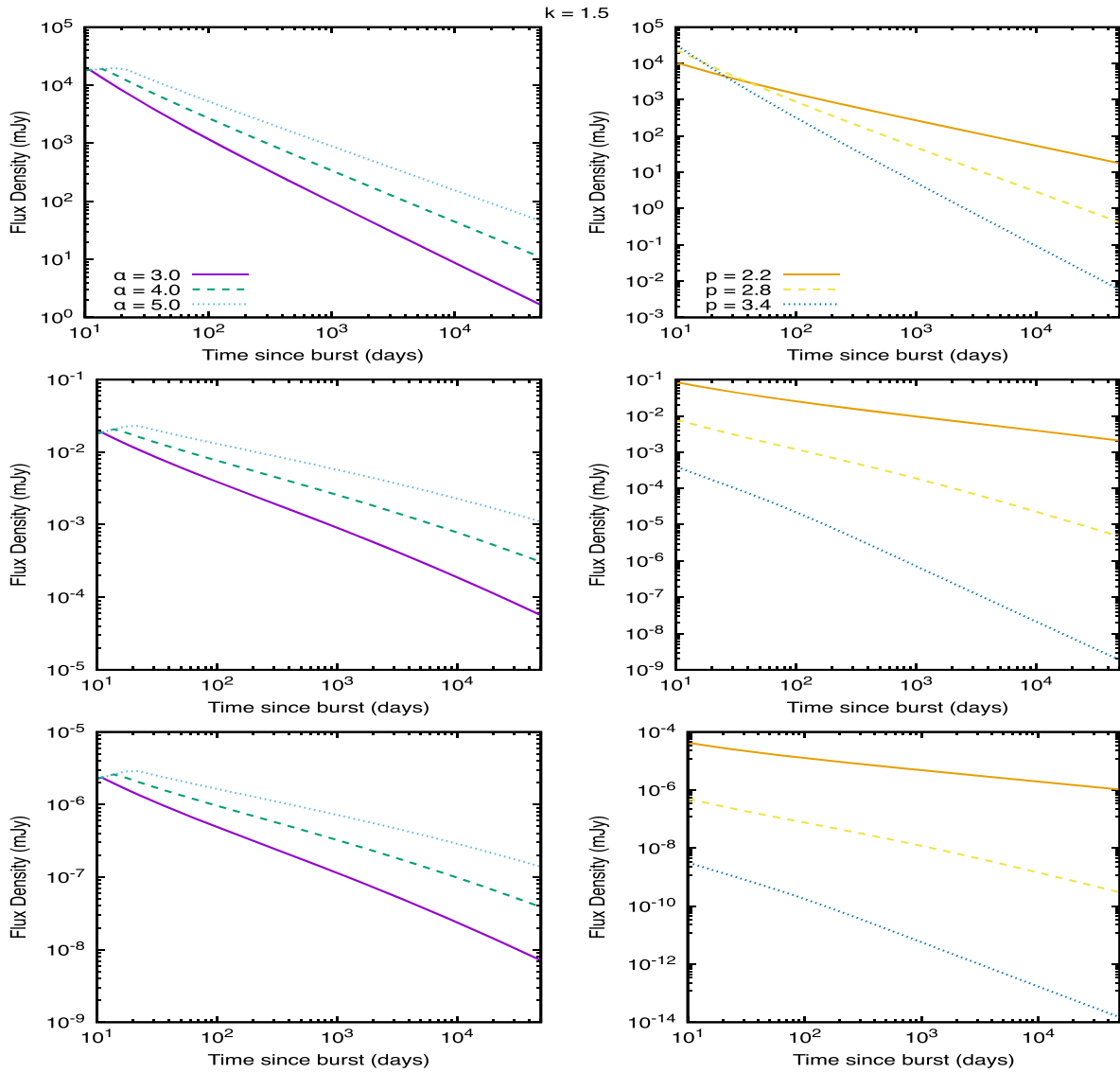
Figure 5. The same as Figure 3, but for $k = 1.5$ with $A_{1.5} = 2.7 \times 10^{28}\,\mathrm{cm}^{-\frac{3}{2}}$.

(Shibata & Taniguchi 2006; Hotokezaka et al. 2013). The disk's kinetic energy and the velocities lie in the ranges of $10^{47} \lesssim \tilde{E} \lesssim 10^{50}\,\mathrm{erg}$ and $0.03 \lesssim \beta\Gamma \lesssim 0.1$, respectively (see, e.g., Dessart et al. 2009; Metzger & Fernández 2014; Fernández et al. 2015).

Cocoon material—The GRB jet will deposit energy as it travels through the neutrino-driven or magnetically driven wind (previously expelled during the merger of two NSs). The energy deposited laterally will produce a cocoon with an energy similar to that of the jet's electromagnetic emission. Murguia-Berthier et al. (2014) looked into the conditions required for cocoon formation as a function of the jet's luminosity. A weak cocoon emission was predicted, regardless of the magnitude of the jet's luminosity. In particular, when Nagakura et al. (2014) numerically examined a low-luminosity jet, the authors concluded that a hot cocoon enclosing the jet would form. The cocoon would break free and spread along the axis of the relativistic jet as soon as it reached the shock breakout material. The external pressure would then drop dramatically beyond the breakout material, allowing the cocoon to accelerate and expand relativistically until it became

transparent. The material mass liberated in the cocoon, the kinetic energy, and the velocities lie in the ranges of $10^{-6} \lesssim M_{\mathrm{ej}} \lesssim 10^{-4}\,M_{\odot}$, $10^{47} \lesssim \tilde{E} \lesssim 10^{50.5}\,\mathrm{erg}$, and $0.2 \lesssim \beta\Gamma \lesssim 10$, respectively (see, e.g., Nagakura et al. 2014; Murguia-Berthier et al. 2014; Lazzati et al. 2017, 2018; Nakar & Piran 2017; Gottlieb et al. 2018a).

Figure 9 shows the synchrotron light curves with energy injection by a spinning magnetized NS remnant and generated by materials ejected from the merger of two NSs such as the dynamical ejecta, the cocoon material, the shock breakout material, and the wind ejecta. The synchrotron light curves correspond to the (from top to bottom) radio (1.6 GHz) and X-ray (1 keV) bands, respectively, for $k = 0$. Taking into account the velocities of the wind and the shock breakout material, we also consider the trans-relativistic (TR; $\beta \sim 0.8$) and deep-Newtonian (DN; $\beta \sim 0.08$) regimes, respectively. The TR and DN timescales during the deceleration phase are given in the Appendix. The light curves are shown for $n = 10^{-2}\,\mathrm{cm}^{-3}$, $\alpha = 3$, $P_0 = 10^{-3}\,\mathrm{s}$, $B = 10^{16}\,\mathrm{G}$, $t_{\mathrm{fb}} = 5 \times 10^9\,\mathrm{s}$, $\epsilon_{\mathrm{B}} = 10^{-2}$, $\epsilon_{\mathrm{e}} = 10^{-1}$, and $p = 2.2$ and the pair of values of $\tilde{E} = 10^{50}\,\mathrm{erg}$ and $\beta = 0.2$ for the dynamical ejecta, $10^{48}\,\mathrm{erg}$
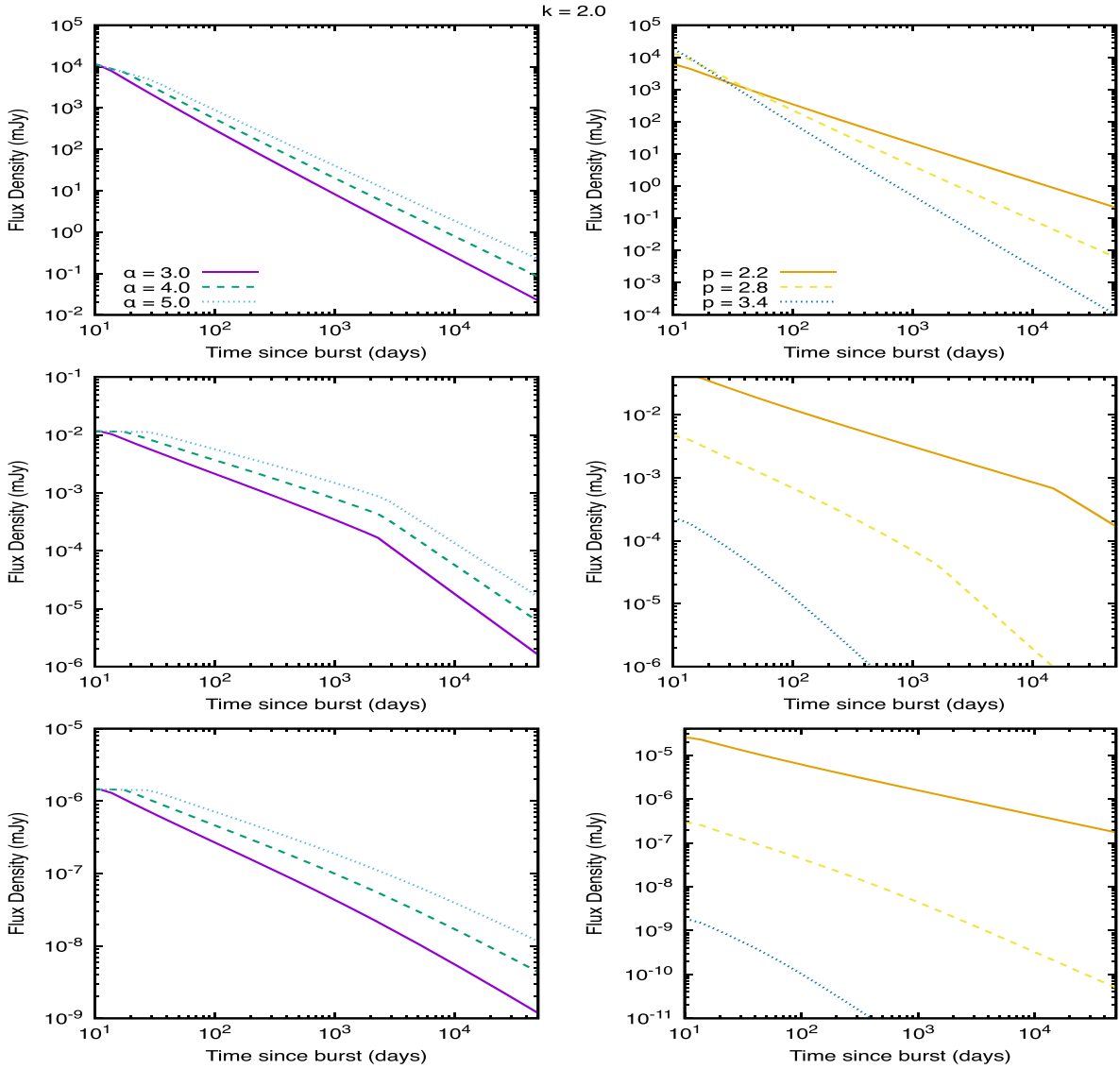
Figure 6. The same as Figure 3, but for $k = 2.0$ with $A_2 = 3 \times 10^{36}$ cm^{-1}.

and 0.3 for the cocoon material, $10^{48.5}$ erg and 0.8 for the shock breakout material, and 10^{50} erg and 0.07 for the wind. Besides, we show for completeness the synchrotron afterglow radiation from an on-axis and off-axis outflow with a viewing angle of $30°$, which are specified in the top panel. The synchrotron light curves from the off-axis outflow are considered as detailed in Fraija et al. (2019b).

The disk wind, the dynamical ejecta, the cocoon, and the shock breakout peak at 1.2×10^5, 7150, 522.5, and 56.1 days, respectively. The total contribution of synchrotron light curves exhibits a brightening once the off-axis emission decreases at a few years, so that, depending on the parameter values and conditions, the synchrotron emission from the ejected materials could be detected or not (see Murguia-Berthier et al. 2014; Nagakura et al. 2014 for the cocoon material).

The top panel shows the evolution of the integrated light curve in the radio band. The early time behavior of the radiation due to the jet's emission is emphasized by showing different solutions for distinct viewing angles. This panel shows that, as the viewing angle is increased, the light curve at early times decreases and takes longer to enter our line of sight. Once the jet enters on-axis, the behavior is independent of the

initial opening angle; however, the light curve becomes dominated by the emission from the other emitted materials.

This last point is highlighted in the subsequent lower panel, where each component's contribution is explicitly plotted. It can be seen that at timescales of $\approx 10^3 - 10^4$ days, the flux density is dominated by the emission from the dynamical ejecta and the shock breakout, while at late times ($\gtrsim 10^5$ days) both the dynamical and the disk wind ejecta have the upper hand as the most influential constituents of the synchrotron light curve. Contrastingly, the cocoon emission lies a couple of orders of magnitude below the other contributions and is not observed.

Figure 10 shows the synchrotron light curves with energy injection produced by a fallback material onto a BH and generated when ejected materials and a relativistic outflow decelerate in a stellar-wind environment. The synchrotron light curves correspond to the (from top to bottom) radio (1.6 GHz) and X-ray (1 keV) bands, respectively for $k = 2$, $A_2 = 3 \times 10^{36}$ cm^{-1} ($A_W = 10$), $t_0 = 1$ s, $t_p = 10^3$ s, $M_{BH} = 2.3\,M_\odot$, $a = 0.7$, $\tau_{vis} = 10^9$ s, $\dot{M}_p = 10^{-6}\,M_\odot$ s^{-1}, $\alpha = 3.0$, $\epsilon_B = 5 \times 10^{-3}$, $\epsilon_e = 10^{-1}$, and $p = 3.2$, and the pair of values 10^{48} erg and 0.3 for the cocoon material, and $10^{48.5}$ erg and 0.8 for the shock breakout material.
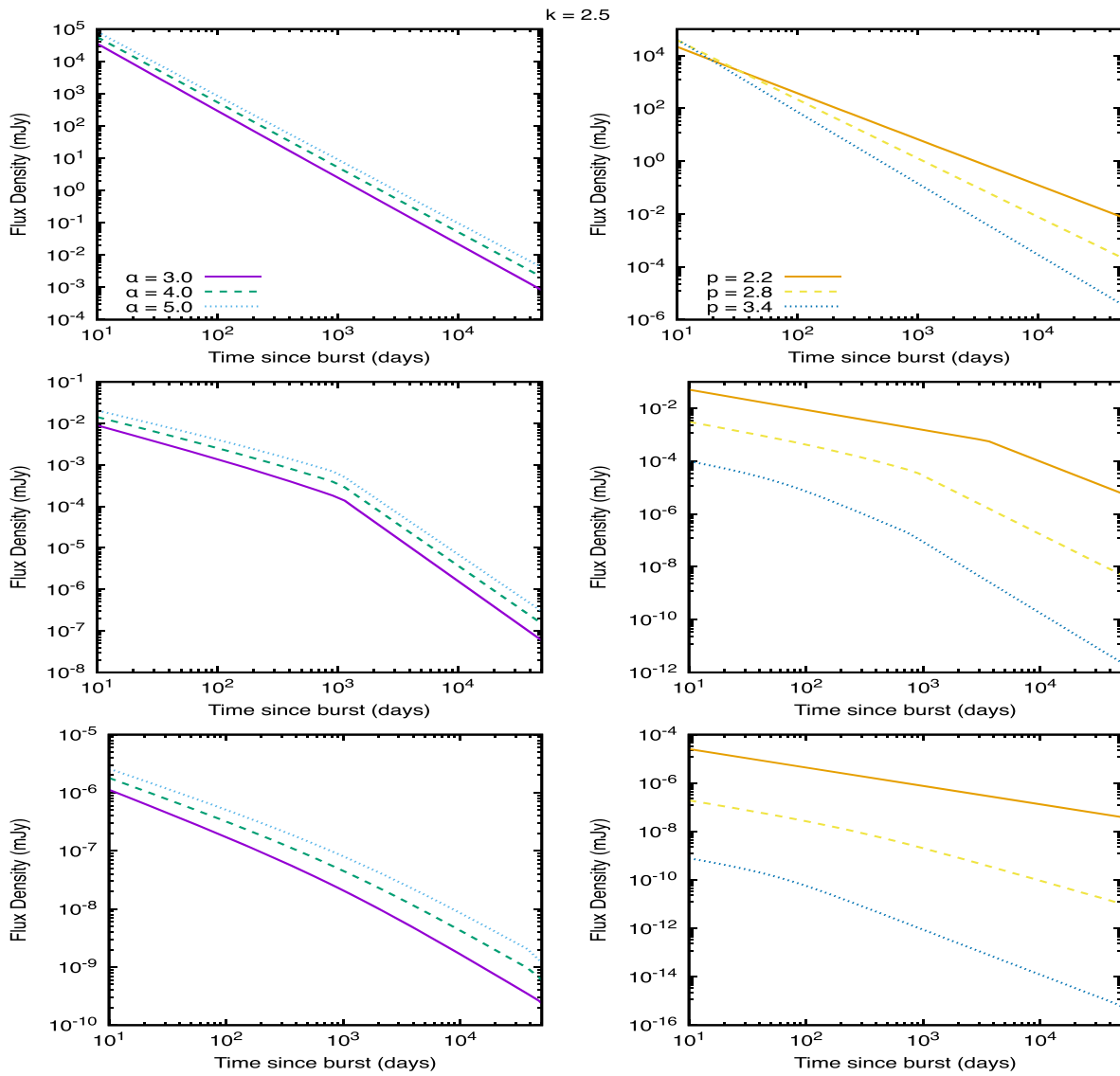
Figure 7. The same as Figure 3, but for $k = 2.5$ with $A_{2.5} = 1.3 \times 10^{45}$ cm$^{-\frac{1}{2}}$.

For a stellar-wind surrounding medium, the jet's contribution to the radio light curve is much shorter than for the case of a constant-density medium, as the top panel shows that it lasts less than a day, while the panels on the left-hand side show that this phase has a duration $\gtrsim 10^3$ days. On the other hand, the light curve at 1 keV shows that the flux density is completely dominated by the jet's emission, as the cocoon's and the shock breakout's contributions lie several orders of magnitude below the jet's. Therefore, a high variation in the behavior of the light curves while comparing the different energy bands could be a hint for an outflow evolving in a medium that is stratified. The synchrotron light curves at the radio bands show that, depending on the parameter values, the afterglow emission from the cocoon and shock breakout materials could be detected at timescales of days. However, if the outflow is chocked, radio fluxes could be detected on timescales of hours.

GRBs could be successful or chocked, this is determined by the range of values in the observables such as luminosity, duration, and bulk Lorentz factor (see, e.g., MacFadyen et al. 2001; Mészáros & Waxman 2001; Murguia-Berthier et al. 2014; Fraija 2014; Nagakura et al. 2014; Sobacchi et al. 2017;

Bromberg et al. 2011). As an indication of this behavior, successful GRBs might be less frequent than choked ones, only limited by the ratio of SNe (Types Ib/c and II) to lGRB rates (Totani 2003; Ando & Beacom 2005). Some SNe of Type Ic BL not connected with GRBs have been suggested to arise from events such as off-axis GRBs or failed jets (see, e.g., Izzo et al. 2019, 2020; Beniamini et al. 2020). One exponent of such a possibility is the failed burst GRB 171205A, which besides being associated with SN 2017iuk, exhibited material with high expansion velocities $\beta \sim 0.4$ interpreted as mildly relativistic cocoon material (Izzo et al. 2019). As another example, in the context of off-axis GRBs that enter on-axis after some time, Izzo et al. (2020) found that the X-ray observations from the nearby SN 2020bvc were consistent with the afterglow emission generated by an off-axis jet with a viewing angle of 23° when it decelerated in a circumburst medium with a density profile with $k = 1.5$. However, as no prompt emission was detected, the authors implied that this was a hint for the first orphan GRB detected through its associated SN emission.

As follows we apply the current model to describe the latest multiwavelength afterglow observations ($\gtrsim 900$ days) of the
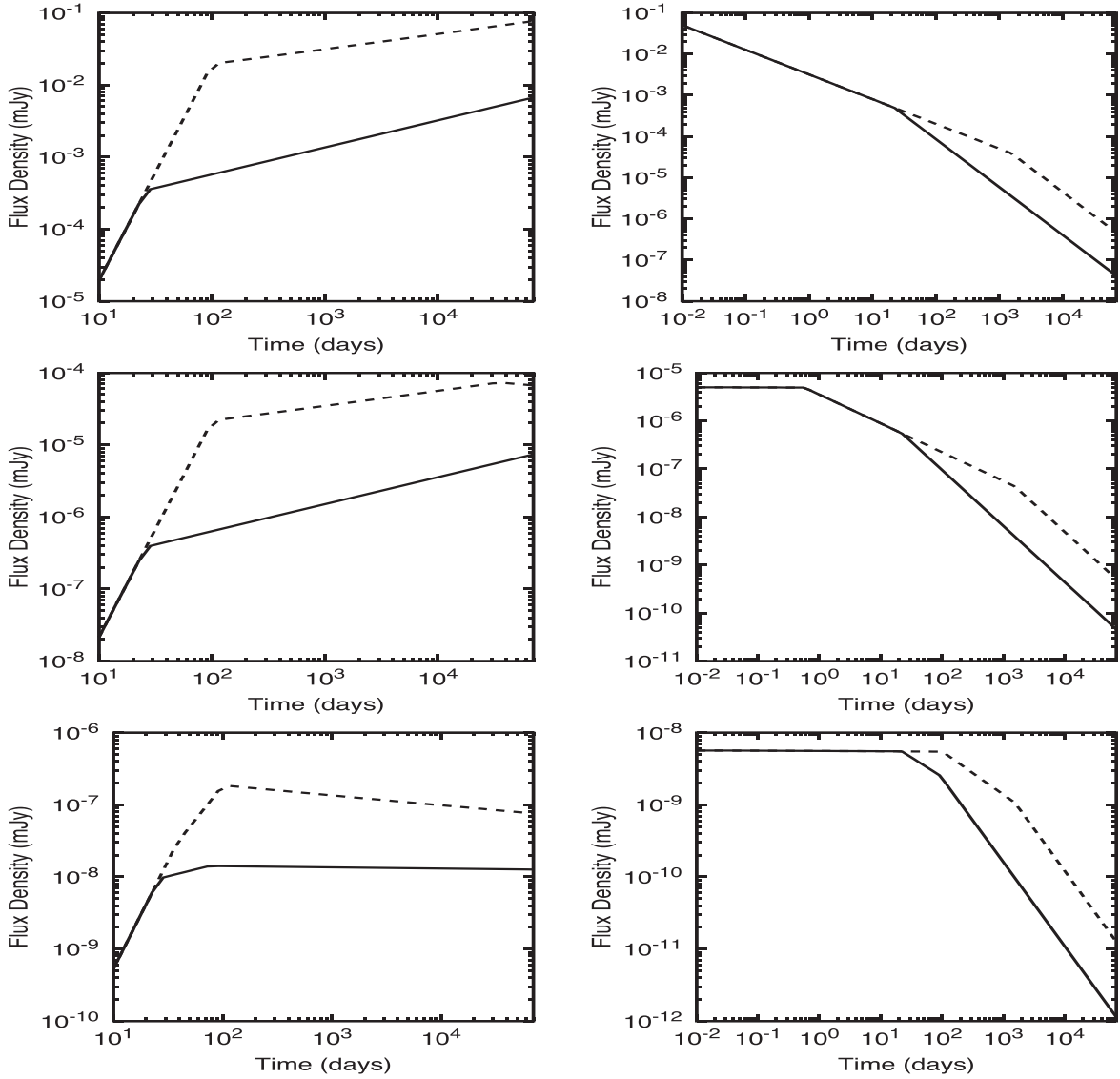
Figure 8. Synchrotron light curves generated by the deceleration of the sub-relativistic ejecta with and without energy injection for a constant density (left; $k = 0$ and $n = 1$ cm^{-3}, $q = 0$) and stellar-wind (right; $k = 2$, and $A_W = 100$, $q = 0.66$) medium. The millisecond magnetar scenario was required in the panels on the left-hand side with the parameter values of $P_0 = 10^{-3}$ s, $B = 10^{14}$ G, and $t_{fb} = 10^3$ s, and the fallback material onto the BH scenario was used in the panels on the right-hand side with the parameter values of $t_0 = 0$ s, $t_p = 10^3$ s, $M_{BH} = 2.3\ M_\odot$, $a = 0.7$, $\tau_{vis} = 10^9$ s, and $\dot{M}_p = 10^{-6}\ M_\odot$ s^{-1}. The panels from top to bottom correspond to the radio (1.6 GHz), optical (R band), and X-ray (1 keV) bands, respectively. The dashed line represents the case of energy injection and the solid line without energy injection. The parameter values used in both panels are $\epsilon_e = 10^{-1}$, $\epsilon_B = 10^{-4}$, $\beta = 0.4$, $\tilde{E} = 10^{51}$ erg, and $\alpha = 3.0$.

GW170817/GRB 170817A event, and using multiwavelength upper limits associated with (i) promising GW events in GWTC-2 and GWTC-3 that could generate electromagnetic emission, (ii) short bursts with the lowest redshifts ($100 \leqslant z \leqslant 200$ Mpc), and (iii) evidence of KNe, we provide constraints on the possible afterglow emission.

5.1. GW170817/GRB 170817A Event

GW radiation from the merger of two NSs (Metzger 2017) is expected together with a short gamma-ray prompt and a UV-optical-IR KN emission in timescales of ~1 s and a few days, respectively (Li & Paczyński 1998; Rosswog 2005; Metzger et al. 2010; Kasen et al. 2013; Metzger 2017). A KN classified as *blue* and *red* is a transient powered by radioactive decay of unstable heavy nuclei via the rapid neutron capture (r-process) synthesized in merger ejecta. The blue KN situated at the polar

regions has low opacity and fast velocity $\beta \simeq 0.3$ and the red KN positioned at the equatorial plane has high opacity due to the lanthanide-bearing matter and slower velocity $\beta \simeq 0.1$ (Metzger & Fernández 2014; Perego et al. 2014; Wanajo et al. 2014; Miller et al. 2019).

As follows, we present the GW170817/GRB 170817A observations, focusing on and describing the latest ones with synchrotron afterglow radiation from a sub-relativistic material, i.e., a KN afterglow emission, and when the spinning magnetized NS remnant is accreting and injecting energy into afterglow. We consider the characteristics of the blue KN as used in Fraija et al. (2021a).

5.1.1. Multiband Observations

On 2017 August 17 12:41:06, the short GRB 170817A was first detected by the Gamma-ray Burst Monitor (GBM)
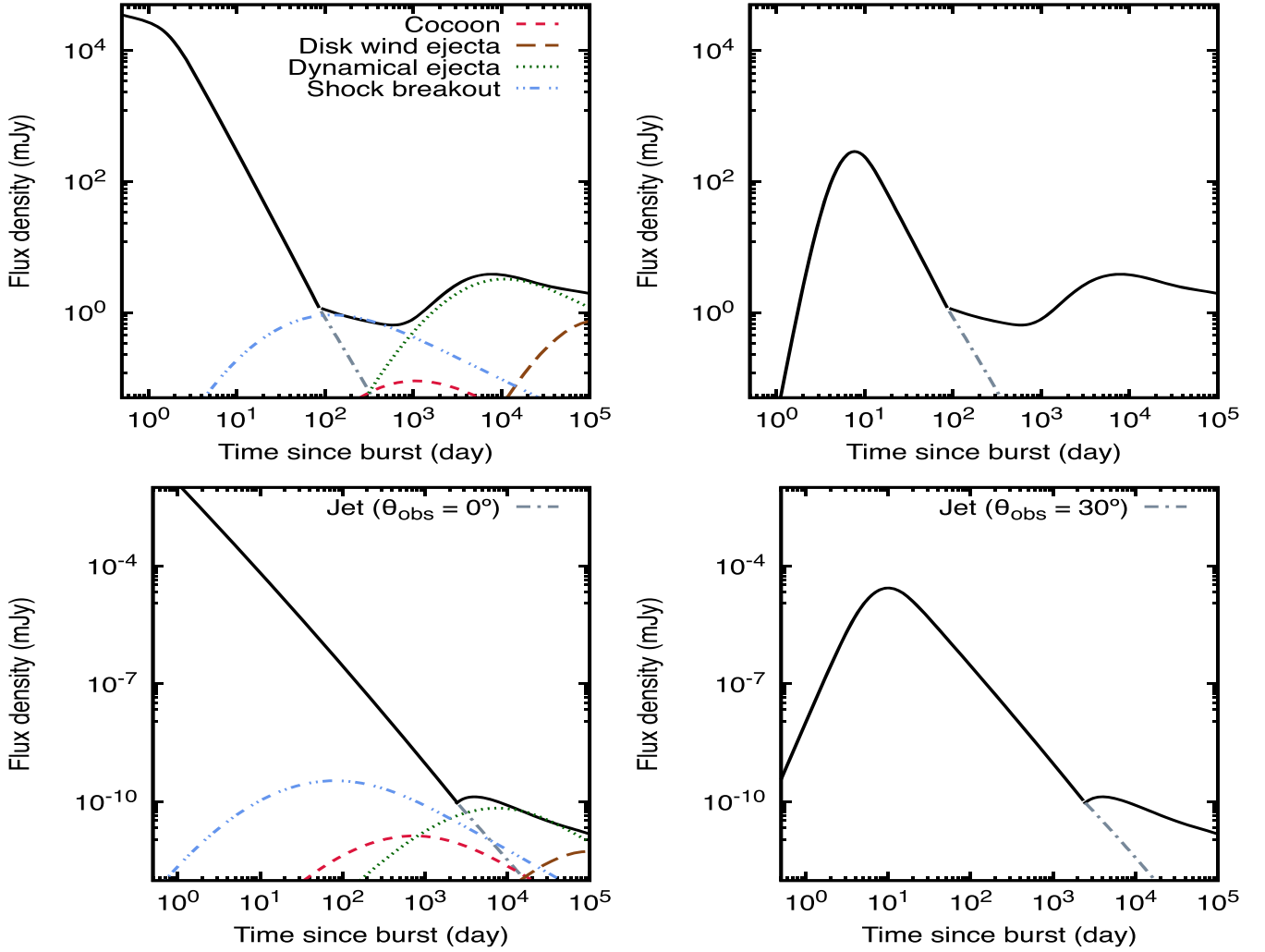
Figure 9. Synchrotron light curves generated by the deceleration of the relativistic jet, cocoon, the shock breakout, the dynamical, and the wind ejecta in the constant-density medium ($k = 0$). The panels on the left-hand side show the light curves from an on-axis jet and the ones on the right-hand side from an off-axis jet with a viewing angle of $30°$. The spinning magnetized NS scenario with the parameter values $P_0 = 10^{-3}$ s, $B = 10^{16}$ G, and $t_{fb} = 5 \times 10^9$ s was used. The upper and lower panels correspond to radio (1.6 GHz) and X-rays (1 keV) bands, respectively. The gray dashed–dotted, the red dashed, brown long-dashed, the green dotted and the blue double-dashed–dotted curves represent the contribution of the relativistic jet, the cocoon, the shock breakout, the dynamical, and the wind ejecta. The values of $\tilde{E} = 10^{50}$ erg, $\epsilon_B = 10^{-2}$, $\epsilon_e = 10^{-1}$, $n = 10^{-2}$ cm^{-3}, $p = 2.2$, and $d_z \approx 100$ Mpc ($z = 0.023$) were used (Fraija et al. 2019b).

instrument onboard the Fermi satellite with a reported location of R.A. $= 176.8$ and decl. $= -39.8$ with an error of $11.6°$ (Goldstein et al. 2017). Approximately 2 s before the GBM trigger, the LIGO Scientific Collaboration and the Virgo Collaboration reported the identification of a GW candidate (GW170817) consistent with the same location of GRB 170817A (Connaughton et al. 2017; Abbott et al. 2017a, 2017b). Relevant evidence soon connected the progenitor of GRB 170817A with the merger of two NSs, being the first detection of GWs from this merger (Abbott et al. 2017a, 2017b).

About 10.9 hr after the GW trigger, this event also exhibited a transient and fading optical source. This optical transient, named the Swope Supernova Survey 2017a, coincident with the quiescent galaxy NGC 4993 at a distance of $d_z = 40.7 \pm 2.36$ Mpc (Cantiello et al. 2018) was associated with KN emission (AT 2017gfo; Soares-Santos et al. 2017; Coulter et al. 2017; Cowperthwaite et al. 2017; Tanvir et al. 2017; Smartt et al. 2017; Gottlieb et al. 2018a). This burst was followed up with an enormous observational campaign covering radio, optical, and X-ray bands (see, e.g., Abbott et al. 2017b, 2017c; Mooley et al. 2018; Lyman et al. 2018; Margutti et al. 2018; Troja et al. 2017;

Alexander et al. 2018; D'Avanzo et al. 2018b, and references therein). The observations of the nonthermal spectrum of GRB 170817A gathered during the first ≈ 900 days after the initial merger were analyzed by several authors and it was shown that they were consistent with synchrotron radiation from an off-axis structured jet decelerated in a constant-density medium. This relativistic jet observed from a viewing angle of $15° \leqslant \theta_{obs} \leqslant 25°$ was described with an opening angle $\theta_j \approx 5°$ (Kasliwal et al. 2017b; Lamb & Kobayashi 2017; Mooley et al. 2018; Fraija et al. 2019a).

Hajela et al. (2022) analyzed the latest X-ray and radio observations of GRB 170817A collected with the Chandra X-ray Observatory, the Very Large Array (VLA), and the MeerKAT radio interferometer about 3.3 yr after the initial merger, and reported evidence of a new X-ray emission component. This new measurement was not in agreement with the synchrotron off-axis afterglow model in constant density. Given these contrasting properties, the authors offered the solution to explain this phenomena in the framework of either radiation from accretion processes on the compact-object remnant or a KN afterglow.
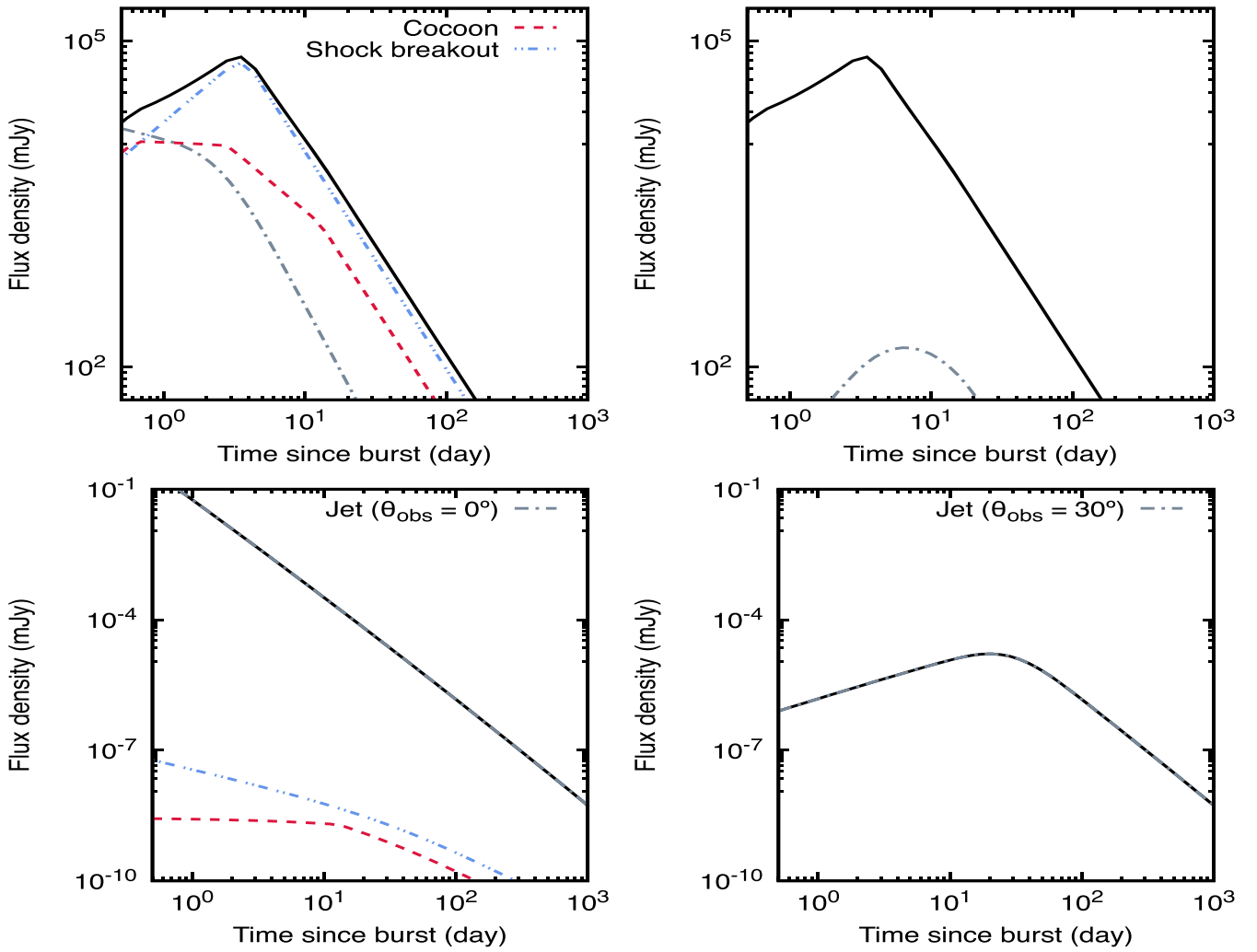
Figure 10. The same as Figure 9, but the deceleration of the cocoon and the shock breakout in the stellar-wind medium ($k = 2$). The fallback material onto the BH scenario with the parameter values $t_0 = 1$ s, $t_p = 10^3$ s, $M_{\rm BH} = 2.3\,M_\odot$, $a = 0.7$, $\tau_{\rm vis} = 10^9$ s, and $\dot{M}_{\rm p} = 10^{-6}\,M_\odot\,{\rm s}^{-1}$ was used.

5.1.2. Analysis, Description, and Discussion

The observations of the nonthermal spectrum of GRB 170817A gathered during the first ≈ 900 days after the initial merger have been modeled with synchrotron forward-shock emission generated by the deceleration of a relativistic off-axis jet (Troja et al. 2017; Kasliwal et al. 2017b; Lamb & Kobayashi 2017, 2018; Resmi et al. 2018; Margutti et al. 2017a), a cocoon (Lazzati et al. 2017; Gottlieb et al. 2018b; Fraija et al. 2019b) and a shock breakout (Gottlieb et al. 2018b; Hotokezaka et al. 2018; Fraija et al. 2019c) in a constant-density medium. While the synchrotron radiation from an off-axis jet peaked at $\approx 110 - 130$ days, the synchrotron radiation from the relativistic cocoon material with a bulk Lorentz factor ($\Gamma_c \gtrsim 4$) increased gradually during the first weeks, after reaching a maximum flux at ~ 15–45 days and decreased afterward (Lazzati et al. 2017; Fraija et al. 2019b). A similar description was performed considering the relativistic shock breakout material (see, e.g., Fraija et al. 2019c). On the other hand, Figure 9 shows that disk wind ejecta peaks at timescales as long as $\approx 10^5$ s (see Equation (A3)). Therefore, we only consider the sub-relativistic decelerated material with the typical parameters of the dynamical ejecta, which peaks at timescales of years (see Equation (A2)), as shown in Figure 9.

We use the X-ray, optical, and radio observations of GRB 170817A used in Fraija et al. (2021a) and Hajela et al. (2022), together with the best-fit curve found by the off-axis jet with the cocoon model, which is introduced in Fraija et al. (2019b). To describe the latest multiband observations through the sub-relativistic decelerated material in a constant-density medium, we constrain the parameter space that reproduces their synchrotron light curves. Figures 11 and 12 show the parameter space allowed for $\beta = 0.3$ and 0.4, respectively. We consider a spinning magnetized NS as the remnant of the merger of two NSs, which is continuously injecting energy into the blast wave due to magnetic spin-down. For a typical value of efficiency $\eta = 0.1$ (Xiao & Dai 2019) and the half-opening angle of the KN AT 2017gfo associated with GW170817 ($\theta_j = 30°$; Dhawan et al. 2020), the luminosity injected into the afterglow becomes similar to the spin-down luminosity. Both figures are displayed as a function of the magnetic field of the NS remnant, the isotropic-equivalent kinetic energy $\tilde{E}$, and the constant-density medium $n = A_0$ that describe the latest multiband observations for values of the synchrotron afterglow model $\epsilon_e = 10^{-1}$, $\epsilon_B = 10^{-3}$, $\alpha = \{3.0, 4.0, 5.0\}$, and $p = \{2.05, 2.15\}$ (Bauswein et al. 2013; Troja et al. 2017; Metzger 2017; Fong et al. 2019; Mooley et al. 2018; Fraija et al. 2019a;
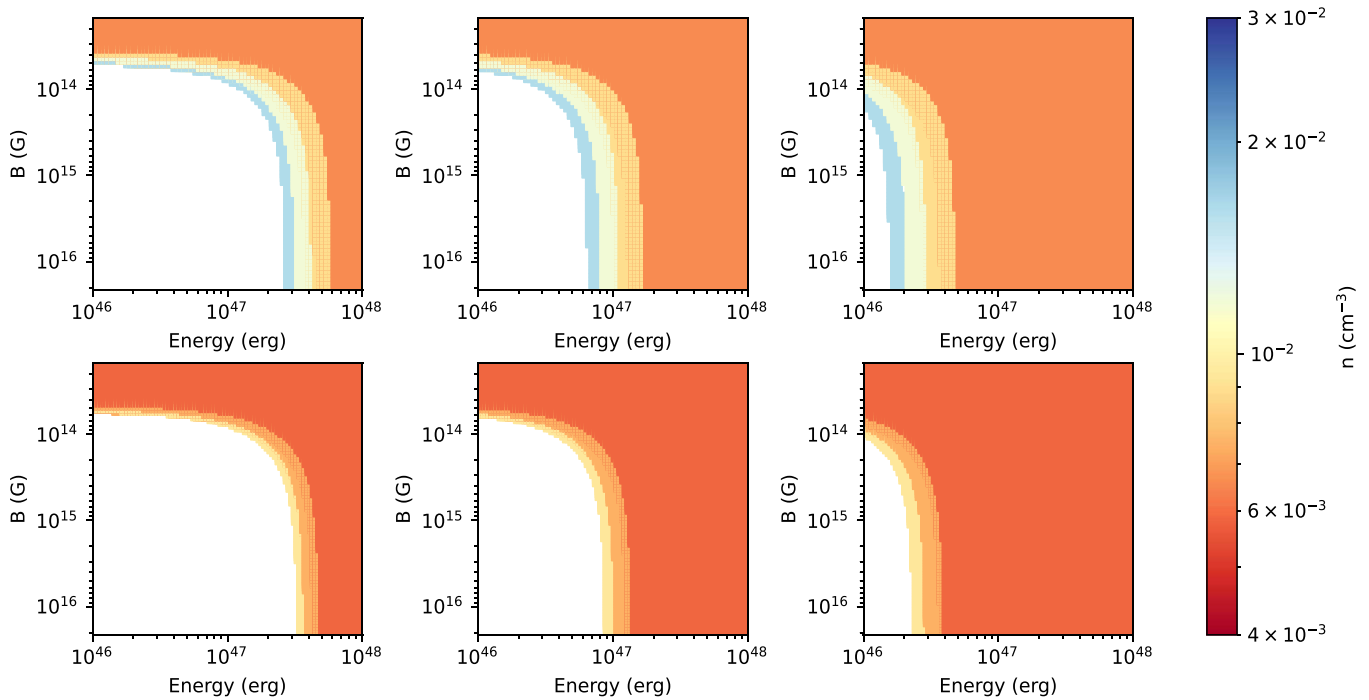
Figure 11. The allowed parameter space of the luminosity injection, isotropic-equivalent kinetic energy, and constant-density medium for $\epsilon_e = 10^{-1}$, $\epsilon_B = 10^{-3}$, $\beta = 0.3$, $p = 2.05$ (upper row), and $p = 2.15$ (lower row), $\alpha = 3$ (left column), $\alpha = 4$ (middle column), and $\alpha = 5$ (right column). The white spaces correspond to the excluded parameters.
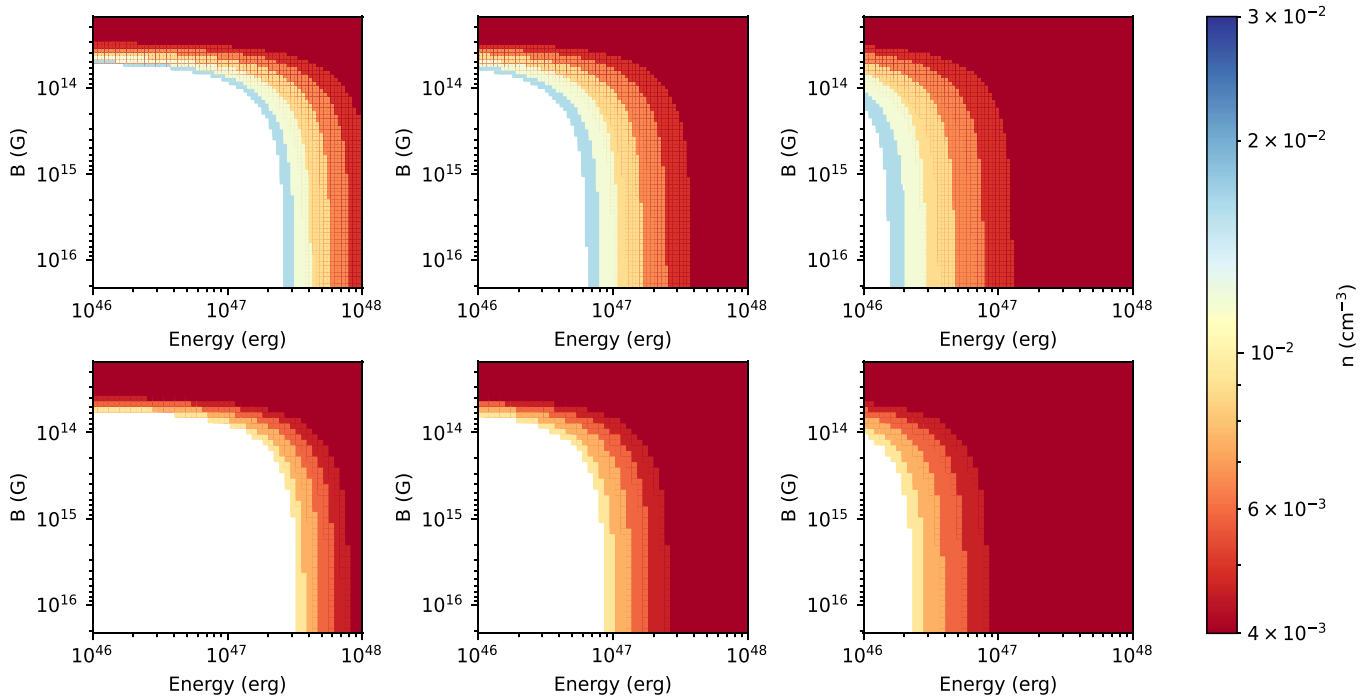

Figure 12. The same as Figure 12, but for $\beta = 0.4$.

Metzger 2019; Kathirgamaraju et al. 2019; Troja et al. 2020; Fraija et al. 2021a). We can see that these parameter spaces are strongly degenerate.

The three columns in Figures 11 and 12 correspond to the values $\alpha = 3.0$, 4.0, and 5.0 from left to right, respectively. In a similar manner, the two rows correspond to the values $p = 2.05$ and 2.15 from top to bottom, respectively. Figure 11 shows that

approximately the same parameter space of the magnetic field and isotropic-equivalent kinetic energy is allowed for both values of the electron energy distribution index p. Nevertheless, there are differences in the allowed values of the circumburst density, as Figure 11 shows that for $p = 2.05$, larger densities ($n \sim 10^{-2}$ cm^{-3}) are preferred, while for $p = 2.15$, densities of the order $n \sim 10^{-3}$ cm^{-3} are favored. On the other hand, upon
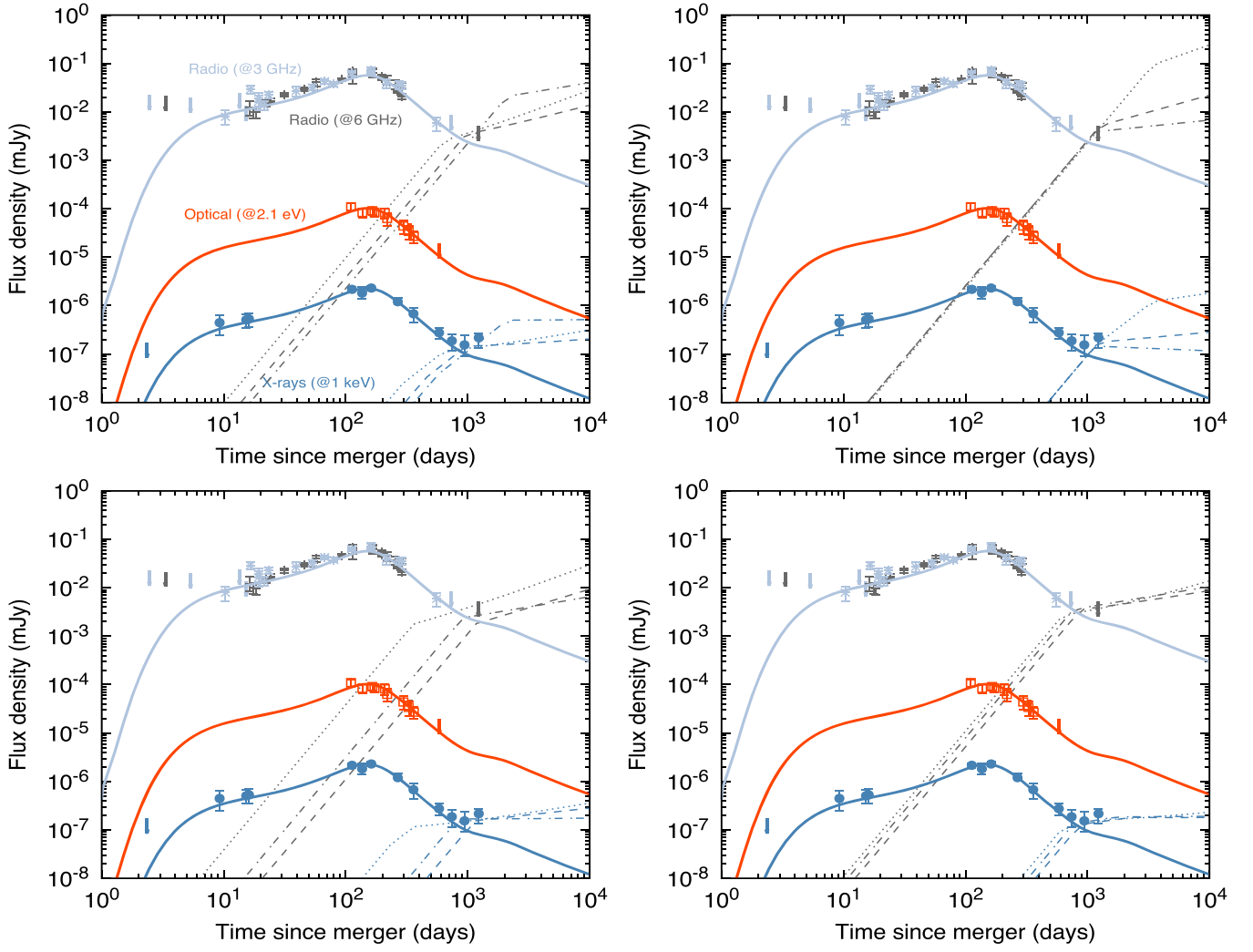
Figure 13. The multiwavelength afterglow observations of GW170817/GRB 170817A at X-rays, optical bands, and radio wavelengths with the best-fit synchrotron light curves from a relativistic structured jet (solid lines; Fraija et al. 2019b) and sub-relativistic material (dotted, dashed, and dotted–dashed lines). The latest X-ray data point and the radio upper limit are taken from Hajela et al. (2022). The synchrotron light curves with energy injection from the deceleration of sub-relativistic material in a constant density are shown in the panels on the left in radio at 3 GHz and X-rays at 1 keV (Cantiello et al. 2018). The millisecond magnetar scenario with accretion is considered in all curves for $P_0 = 10^{-3}$ s and $t_{fb} = 10^9$ s. The parameters used for the curves in the above panels are (left) $\beta = 0.3$, $p = 2.05$, $\epsilon_B = 10^{-4}$, and $\epsilon_e = 10^{-1}$; (dotted lines) $\tilde{E} = 10^{46}$ erg, $B = 1.5 \times 10^{13}$ G, $n = 6.61 \times 10^{-3}$ cm^{-3}, and $\alpha = 3$; (dashed lines) $\tilde{E} = 3.93 \times 10^{46}$ erg, $B = 6.5 \times 10^{13}$ G, $n = 8.88 \times 10^{-3}$ cm^{-3}, and $\alpha = 4$; (dashed–dotted lines) $\tilde{E} = 10^{46}$ erg, $B = 1.3 \times 10^{14}$ G, $n = 1.60 \times 10^{-2}$ cm^{-3}, and $\alpha = 5$; (right) $\beta = 0.3$, $p = 2.15$, $\epsilon_B = 10^{-3}$, and $\epsilon_e = 10^{-1}$; (dotted lines) $\tilde{E} = 10^{46}$ erg, $B = 4.8 \times 10^{13}$ G, $n = 5.87 \times 10^{-3}$ cm^{-3}, and $\alpha = 3$; (dashed lines) $\tilde{E} = 1.9 \times 10^{47}$ erg, $B = 3.2 \times 10^{15}$ G, $n = 5.87 \times 10^{-3}$ cm^{-3} and $\alpha = 4$; and (dashed–dotted lines) $\tilde{E} = 10^{48}$ erg, $B = 2.7 \times 10^{13}$ G, $n = 5.87 \times 10^{-3}$ cm^{-3}, and $\alpha = 5$. The parameters used for curves of the lower panels are (left) $\beta = 0.4$ $p = 2.05$, $\epsilon_B = 10^{-3}$, and $\epsilon_e = 10^{-1}$; (left) $\tilde{E} = 3.1 \times 10^{47}$ erg, $B = 5.4 \times 10^{13}$ G, $n = 2.72 \times 10^{-3}$ cm^{-3}, and $\alpha = 3$; (dashed lines) $\tilde{E} = 4.73 \times 10^{47}$ erg, $B = 4.2 \times 10^{14}$ G, $n = 1.51 \times 10^{-3}$ cm^{-3}, and $\alpha = 4$; (dashed–dotted line) $\tilde{E} = 10^{46}$ erg, $B = 1.1 \times 10^{14}$ G, $n = 1.61 \times 10^{-2}$ cm^{-3}, and $\alpha = 5$; (right) $\beta = 0.4$ $p = 2.15$, $\epsilon_B = 10^{-3}$, and $\epsilon_e = 10^{-1}$; (dotted line) $\tilde{E} = 9.10 \times 10^{47}$ erg, $B = 4.7 \times 10^{15}$ G, $n = 3.66 \times 10^{-3}$ cm^{-3}, and $\alpha = 3$; (dashed lines) $\tilde{E} = 4.09 \times 10^{46}$ erg, $B = 4.3 \times 10^{13}$ G, $n = 2.89 \times 10^{-3}$ cm^{-3}, and $\alpha = 4$; and (dashed–dotted lines) $\tilde{E} = 1.45 \times 10^{46}$ erg, $B = 5.7 \times 10^{13}$ G, $n = 4.64 \times 10^{-3}$ cm^{-3}, and $\alpha = 5$.

the increase of α, it is shown that the 3D parameter space shrinks, which means that smaller values of α are able to give stronger constraints on the rest of the parameters.

Figure 12 is the same as 11, but it considers $\beta = 0.4$. Overall, the regions of allowed energy and magnetic field parameter space are very similar to the ones in Figure 11 and the same behavior as described in the previous paragraph can be observed. The main difference between both figures is that for $\beta = 0.4$ lower number densities are preferred, as shown by the deeper red color of the plots. For both values of velocity ($\beta = 0.3$ and 0.4), $t_{fb} = 5 \times 10^9$ s, and $10^{13.7} \lesssim B \lesssim 10^{16.3}$ G, the values of $p = 2.15$, $n < 5 \times 10^{-3}$ cm^{-3}, and $\alpha = 5$ are preferred, although the value of $\alpha = 3.0$ is not discarded.

Figure 13 shows the multiband afterglow observations of GRB 170817A, the best-fit curve from a relativistic structured off-axis jet (solid lines; Fraija et al. 2019b), and several allowed curves (dotted, dashed, and dashed–dotted lines) from the sub-relativistic material shown in this work. The afterglow observations are shown at X-rays, optical bands, and radio wavelengths, and the synchrotron light curves are obtained at 1 keV (blue), 2.1 eV (red), 6 GHz (black), and 3 GHz (gray). In each panel we consider the PL indexes $\alpha = 3.0$ (dotted line), 4.0 (dashed line), and 5.0 (dashed–dotted line) for $\beta = 0.3$ (panels above) and $\beta = 0.4$ (panels below) with $p = 2.05$ (left) $p = 2.15$ (right). We can see that for different sets of parameters, we can obtain similar results about the description

of the latest observations. It indicates, as expected, that our results are not unique but are possible solutions because the synchrotron equations are degenerate in these parameters.

It is relevant to mention that the value of the mean opacity for which the KN ejecta is transparent $k_s \approx \beta_{-1}^2 M_{ej,-1.3}^{-1} t_{th,3}^2 \approx 10^{3.5}\,\mathrm{g}^{-1}\,\mathrm{cm}^2$ agrees with the radiation transfer simulations, which is $\gtrsim 10\,\mathrm{g}^{-1}\,\mathrm{cm}^{-2}$ for lanthanide-rich ejecta (Barnes & Kasen 2013; Tanaka & Hotokezaka 2013; Shibata & Hotokezaka 2019). The luminosity would be estimated as $L_{bol} \approx 10^{38}\,\mathrm{erg}\,\mathrm{s}^{-1}\,t_{th,3}^{1.3}M_{ej,-1.3}$ (Shibata & Hotokezaka 2019), where t_{th} is the timescale when the KN eject enters the thin regime. It is worth noting that the features of the synchrotron emission of the sub-relativistic material are consistent with the faster *blue* KN afterglow.

We have considered the spinning magnetized NS scenario and discarded the fallback material on the BH scenario proposed in Section 3.2 because the rate of fallback accretion estimated at early times with the parameters used to describe the latest observations are fully different from the rate of fallback accretion used in hydrodynamical simulations (see, e.g., MacFadyen et al. 2001; Zhang et al. 2008). It can be demonstrated as follows. At $t = t_p = 1000$ days, the expectation accretion rate and the BZ luminosity (Equation (20)) are $\dot{M}_{BH} \approx \dot{M}_p(t/t_p)^{-5/3}$ with $\tau_{vis} \approx t_p$ and $L_{BZ} \approx 10^{39}\,\mathrm{erg}\,\mathrm{s}^{-1}\,G(a)\dot{M}_{p,-2}(t\ 10^{-3}\,\mathrm{days})^{-5/3}$, respectively. The previous derivation is similar to the result found by Hajela et al. (2022) after modeling the latest observations at 10^3 days. However, extrapolating the rate of fallback accretion at early times ~ 1 s, it would be $\dot{M}_{fb} \approx 10^{-17}\,M_\odot\,\mathrm{s}^{-1}$, which is different from the rate of fallback accretion used in hydrodynamical simulations (see, e.g., MacFadyen et al. 2001; Zhang et al. 2008). It is worth noting that in the BH scenario the rate of fallback accretion at early times is $\propto (t/t_p)^{1/2}$ instead of $(t/t_p)^{-5/3}$, as considered by Hajela et al. (2022).

5.2. Short GRBs with Evidence of a KN

Candidates discussed in the literature with evidence of a KN emission are GRB 050709 (Jin et al. 2016), GRB 060614 (Yang et al. 2015), GRB 130603B (Tanvir et al. 2013; Berger et al. 2013), and GRB 160821B (Kasliwal et al. 2017a; Troja et al. 2019). As follows, we present the four claimed KN observations, and then we show the synchrotron light curves with a set of allowed and ruled out parameters, assuming the characteristics of the blue KN.

5.2.1. Multiband Observations

GRB 050709—GRB 050709 was detected on 2005 July 9 at 22:36:37 UT by the Soft X-Ray Camera, the Wide-Field X-Ray Monitor, and the French Gamma Telescope instruments onboard the High Energy Transient Explorer 2 satellite with a reported location of R. A. $= +23^h01^m30^s$, decl. $= -38°58'33''$ (J2000) (Villasenor et al. 2005). The prompt emission had an approximate duration of 0.5 s in the form of a hard spike in the 3400 keV energy band, which was followed by an extended X-ray emission lasting ~ 130 s (Jin et al. 2016). The accurate location of the burst led to the first-ever identification of the optical afterglow of a short-hard burst in ground-based experiments and the Hubble Space Telescope (Hjorth et al. 2005; Fox et al. 2005). This, in turn, led to the determination of its host galaxy, which lay at redshift $z = 0.16$.

GRB 060614—GRB 060614 was detected on 2006 June 14 at 12:43:48 UT by the Swift-BAT instrument. Its location was found to be at R. A. $= +21^h23^m27^s$, decl. $= -53°02'02''$ (J2000). The event had a duration of 102 s in the $15-350$ keV energy range, which places this burst in the long GRB category (Gehrels et al. 2006). However, subsequent observations showed that the event lacked an associated supernova, which is expected for lGRBs and that its temporal lag and peak luminosity were in line with those of sGRBs (Jin et al. 2016). This contrasting behavior led to denoting GRB 060614 as a *hybrid GRB*.

GRB 130603B—GRB 130603B was simultaneously detected on 2013 June 3 at 15:49:14 UT by Swift-BAT and by Konus-Wind (Tanvir et al. 2013). Its location was found to be at R. A. $= +21^h23^m27^s$, Dec $= -53°02'02''$ (J2000). According to the BAT instrument, it had a duration of $T_{90} \approx 0.18 \pm 0.02$ s in the 15–350 keV band (Barthelmy et al. 2013), which places it in the sGRB class. Optical and near-IR observations of the event were performed which demonstrated the presence of excess near-IR emission matching a KN (Berger et al. 2013).

GRB 160821B—GRB 160821B was detected on 2016 August 21 at 22:29:13 UT by the Swift-BAT instrument (Acciari et al. 2021). The proposed host galaxy's location was found to be at R. A. $= +18^h39^m53.968^s$, decl. $= 62°23'34.35''$ (J2000) at redshift $z = 0.162$, making this GRB one of the lowest redshift bursts observed by Swift (Lamb et al. 2019). It had a duration of $T_{90} = 0.48 \pm 0.07$ s in the 15,350 keV energy band (Troja et al. 2019), which places it in the sGRB class. Upon analysis of the X-ray light curves, Troja et al. (2019) found that there is evidence for continued energy injection from a long-lived central engine. On the other hand, the optical and near-IR observations showed behavior consistent with a KN.

5.2.2. Analysis and Description

Figure 14 presents four columns, where each one corresponds to a different short GRB with evidence of KN emission. Each panel shows the multiband afterglow observations of bursts with evidence of a KN emission and the synchrotron light curves from the cocoon (upper) with $\beta = 0.3$ and the shock breakout (lower) with $\beta = 0.8$ decelerating in a constant-density medium with $n = 1\,\mathrm{cm}^{-3}$ (dashed lines) and $10^{-2}\,\mathrm{cm}^{-3}$ (dotted lines). The synchrotron light curves are presented at 1 keV (blue), R band (gold), and 5 GHz (green). The disk wind and dynamical ejecta are not displayed because these decelerated materials peak at timescales longer than $\approx 10^3$ days, and the multiband afterglow observations with the respective upper limits are reported at timescales from days to ~ 1 month. We consider a spinning magnetized NS with accretion as the remnant of the merger of two NSs. The parameter values used are $P_0 = 10^{-3}$ s, $B = 7 \times 10^{14}$ G, $t_{fb} = 5 \times 10^5$ s, $\tilde{E} = 2.1 \times 10^{49}$ erg, $\epsilon_e = 0.3$, $\epsilon_B = 0.1$, $p = 2.05$, and $\alpha = 3.0$. For GRB 050709, the synchrotron emission at the F814W band from the shock breakout material with a velocity $\beta = 0.8$ is ruled out for both $n = 1\,\mathrm{cm}^{-3}$ and $10^{-2}\,\mathrm{cm}^{-3}$, but not for the cocoon material. For GRB 060614, the synchrotron emission at the R band from the shock breakout material is ruled out for both $n = 1\,\mathrm{cm}^{-3}$ and $10^{-2}\,\mathrm{cm}^{-3}$, but not for the cocoon material. For GRB 130603B, the synchrotron curves from the shock breakout and cocoon are allowed at all bands. For GRB 160821B, the synchrotron curves at 5 GHz and the R band from the cocoon material are ruled out for a density of $n = 1\,\mathrm{cm}^{-3}$, but not for $n = 10^{-2}\,\mathrm{cm}^{-3}$. The
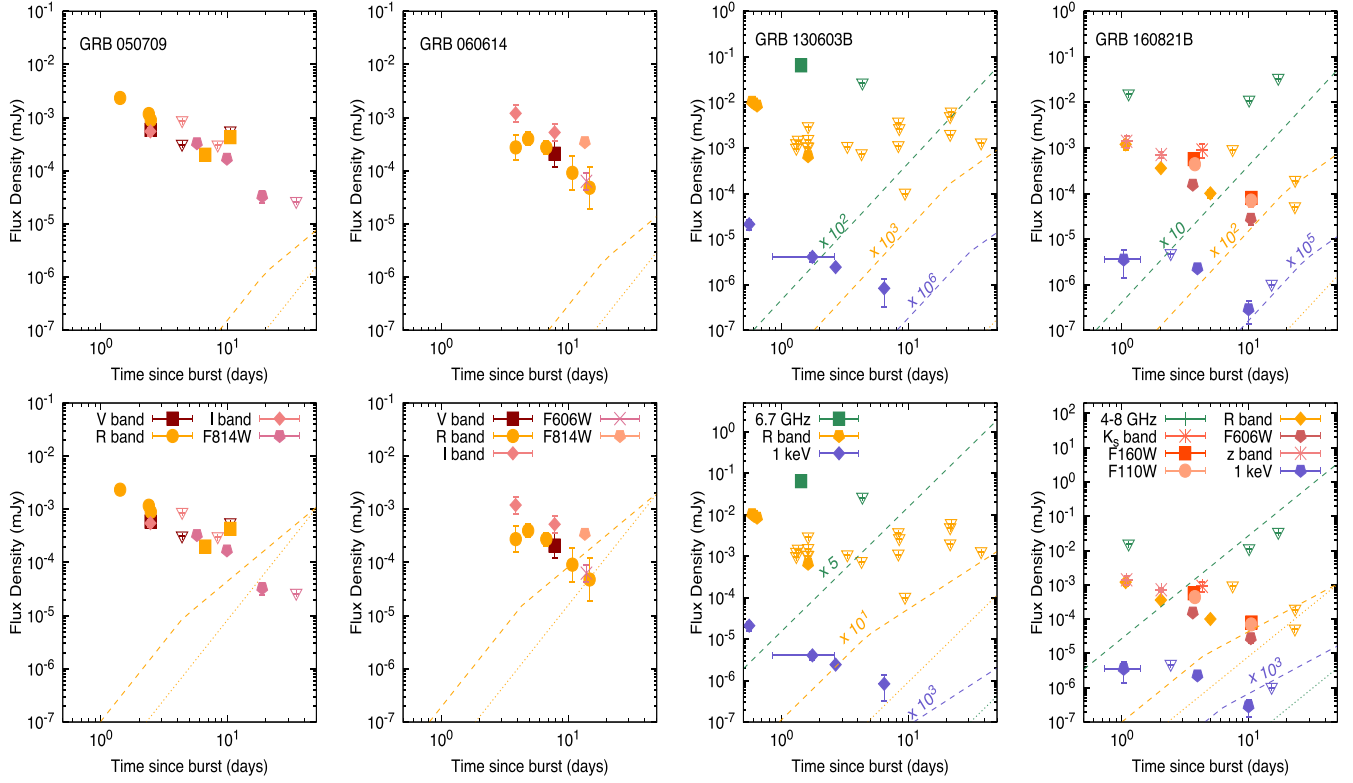
Figure 14. Multiband afterglow observations of sGRBs with evidence of a KN emission and the synchrotron light curves from the cocoon (upper panels; $\beta = 0.3$) and the shock breakout (lower panels; $\beta = 0.8$) materials decelerating in a constant-density medium with $n = 1 \, \mathrm{cm}^{-3}$ (dashed lines) and $10^{-2} \, \mathrm{cm}^{-3}$ (dotted lines). The synchrotron light curves are shown in the X-ray (1 keV; blue), optical (R band; gold), and radio (5 GHz; green) bands. The parameter values used are $P_0 = 10^{-3}$ s, $B = 7 \times 10^{14}$ G, $t_{\mathrm{fb}} = 5 \times 10^5$ s, $\tilde{E} = 1.29 \times 10^{51}$ erg, $\epsilon_{\mathrm{e}} = 0.3$, $\epsilon_{\mathrm{B}} = 0.1$, $p = 2.05$, and $\alpha = 3.0$.

synchrotron curves at 1 keV from the shock breakout and cocoon are allowed. Similarly, all synchrotron curves from the cocoon are allowed. The value of the uniform-density medium with $n = 1 \, \mathrm{cm}^{-3}$ is ruled out in our model for GRB 050709, GRB 060614, and GRB 160821B, but not for GRB 130603B. This result is consistent with the mean value reported for sGRBs (see, e.g., Berger 2014).

Continuous energy injection by the progenitor on the afterglow could generate a long-lived reverse shock at very long timescales, and shocked-accelerated electrons in this region would radiate modifying the forward-shock light curves, as found in some GRB afterglows (see, e.g., Chevalier & Fransson 2006; van der Horst et al. 2007, 2014; Laskar et al. 2018). In a forthcoming manuscript, we will present a detailed analysis of this long-lived reverse shock scenario.

6. Summary

We have extended the synchrotron model presented in Fraija et al. (2021a) and presented the dynamics of deceleration of a sub-relativistic material when the central engine (a remnant of either a spinning magnetized NS or a fallback material onto a BH) injects energy into the blast wave and the external medium is stratified with a density profile $A_k r^{-k}$ with $0 \leqslant k \leqslant 2.5$. We have considered different profiles of the energy injection and also GRB progenitors. The energy injection index $q = 0$ is connected with a spinning magnetized NS and q, in general, with fallback material onto a central BH. The total isotropic-equivalent kinetic energy was introduced as the superposition of the energy distribution E_β and the energy injection E_t. When the condition $E_t \ll E_\beta$ is satisfied, the synchrotron light curve

mimics the ones without energy injection. Otherwise, for $E_t \ll E_\beta$ the continuous energy injection into the afterglow dominates and many differences are observed. The constant-density medium ($k = 0$) is associated with the death of massive stars and the merger of two NSs, and the stratified medium ($1 \leqslant k \leqslant 2.5$) is only expected with the death of massive stars. We have presented the synchrotron light curves in radio at 1.6 GHz, optical at the R band, and X-rays at 1 keV with typical values of GRB afterglows and the scenarios of spinning magnetized NS and fallback material onto BH with different characteristic timescales for a generic remnant located at $d_z = 100$ Mpc.

The synchrotron light curves exhibit the maximum flux on timescales from days to years, although if the remnant injects large amounts of energy, the maximum flux could be expected on timescales of hours. These light curves exhibit that, during the early stages, there is an increase in the flux. During this epoch, when the sub-relativistic ejecta decelerates in a constant-density medium, the light curve grows steeply. For more stratified media, this growth is not as evident. For instance, in the light curves with a density profile with $k = 2.5$, the early time behavior is more gradual. This result implies that if such a flattening or rebrightening at timescales from months to years in the light curve was observed together with GW detection, then this would be associated with the deceleration of a sub-relativistic material launched during the merger of two NSs. Otherwise, we showed that an observed flux that gradually decreases on timescales from months to years could be associated with the deceleration of a sub-relativistic material launched during the death of a massive star with different mass-loss evolution at the end of its life. We have shown that

variations of the stratification parameter are more apparent in the radio light curve when compared to the other fluxes in the other energy bands. This change in the density profile is also more easily appreciated for large values of α, (i.e., $\alpha = 4.0$ and 5.0). Therefore, a transition between density profiles will be more easily observed in the radio band with high values of α.

The two NS merger ejects sub-relativistic material with distinct velocities, which are decelerated by the external medium, generating the synchrotron light curves at different frequencies peaking at timescales from days to years. It is important to mention that before the ejected materials are in the sub-relativistic regime, these might begin momentarily in the TR regime (i.e., with $\beta \sim 0.8$). Similarly, they could finally with the passage of time ($\sim 10^3$ yr) lie in the DN regime with a velocity of $\beta \sim 0.08$. Therefore, we have introduced timescales in both regimes. For instance, with the values of parameters used we have shown that the dynamical ejecta, the cocoon, the shock breakout, and the wind peak at 7150 days, 522.5 days, 56.1 days, and 321.8 yr, respectively. The total contribution of synchrotron light curves exhibits a brightening once the off-axis emission decreases at a few years, so that, depending on the parameter values and conditions, the synchrotron emission from the sub-relativistic materials could be detected or not. The synchrotron light curves could be associated with GW detections. We showed that, in the case of a failed or an off-axis GRB, the nonthermal emission generated by the deceleration of sub-relativistic materials could be detected at early times. In the case of an on-axis GRB, the afterglow emission originated from the deceleration of the relativistic jet would have to decrease substantially so that the afterglow emission from the sub-relativistic ejecta could be observed. In addition, we provided an important tool to distinguish the afterglow emission among the sub-relativistic materials from the relativistic jet through the evolution of the synchrotron flux.

We have applied our model to describe the latest multiwavelength afterglow observations (>900 days) of GW170817/GRB 170817A, and constraints on the afterglow emission of some short bursts with evidence of KNe. Regarding the GW170817/GRB 170817A event, we have constrained the parameter space that reproduces the synchrotron light curves evolving in a constant-density medium from the faster blue KN afterglow. We have considered a spinning magnetized NS as a remnant of the merger of two NSs, which is continuously injecting energy due to spin-down luminosity into the blast wave. We plot the parameter space that describes the X-ray observations and is below the radio upper limits as a function of $\epsilon_e = 10^{-1}$, $\epsilon_B = 10^{-3}$, $\alpha = \{3.0, 4.0, 5.0\}$, and $p = \{2.05, 2.15\}$. We have shown that for both values of velocity ($\beta = 0.3$ and 0.4), $t_{fb} = 5 \times 10^9$ s and $10^{13.7} \lesssim B \lesssim 10^{16.3}$ G, the values of $p = 2.15$, $n < 5 \times 10^{-3}$ cm^{-3}, and $\alpha = 5$ are preferred, although the value of $\alpha = 3.0$ cannot be discarded. The value allowed of $\alpha = 3.0$ in our theoretical model agrees with the values found in numerical simulations (see, e.g., Bauswein et al. 2013) and used for describing the KN emission (Metzger 2017, 2019), and $\alpha = 5.0$ is more consistent with those reported in Kathirgamaraju et al. (2019); Hajela et al. (2022). It is worth noting that the features of the synchrotron emission of the sub-relativistic material are consistent with the faster blue KN afterglow.

Appendix
Deceleration Timescales and Synchrotron Light Curves

A.1. Different Deceleration Timescales

Due to the fact that materials ejected from the merger of two NSs and the gravitational collapse have an ample range of velocities, we consider in addition to this subsection the TR and DN regimes.

TR regime—In this regime, the kinetic energy of the shock in a stratified medium is given by $E = \frac{4\pi}{3}\sigma m_p \beta^2 \Gamma^2 A_k r^{3-k}$ (Blandford & McKee 1976), where the parameter σ is a function of velocity ($\sigma = 0.73 - 0.38\beta$; Huang et al. 1998). The deceleration time becomes

$$t_{\mathrm{dec,TR}} \simeq 23.1 \text{ days}\left(\frac{1+z}{1.022}\right)^{\frac{3-k}{2+q-k}}$$
$$\times A_0^{-\frac{1}{2+q-k}} E_{49}^{\frac{1}{2+q-k}} \beta_{-0.1}^{-\frac{\alpha+5-k}{2+q-k}} \Gamma^{-\frac{\alpha+2}{2+q-k}}. \quad (A1)$$

When the bulk Lorentz factor $\Gamma \to 1$, the TR timescale approaches the Newtonian timescale.

Sub-relativistic (Newtonian) regime—In this regime, the kinetic energy of the shock follows the sub-relativistic spherically symmetric Sedov–Taylor solution. The deceleration time (from Equation (9)) becomes

$$t_{\mathrm{dec}} \simeq 1.3 \times 10^3 \text{ days}\left(\frac{1+z}{1.022}\right)^{\frac{k-3}{k-(q+2)}}$$
$$\times \beta_{-0.3}^{\frac{\alpha+5-k}{k-(q+2)}} A_0^{\frac{1}{k-(q+2)}} E_{51}^{-\frac{1}{k-(q+2)}}. \quad (A2)$$

DN regime—In this regime, the Lorentz factor of the lowest-energy electrons is $\gamma_m \simeq 2$ (Sironi & Giannios 2013; Kathirgamaraju et al. 2016; Margalit & Piran 2020). Using Equation (A4), the deceleration time in this regime becomes

$$t_{\mathrm{dec,DN}} \simeq 1.1 \times 10^5 \text{ days}\left(\frac{1+z}{1.022}\right)^{\frac{3-k}{2+q-k}}$$
$$\epsilon_{e,-1}^{\frac{\alpha+5-k}{2(q+2-k)}} A_0^{-\frac{1}{q+2-k}} E_{51}^{\frac{1}{q+2-k}}. \quad (A3)$$

In this case, the value of velocity is $\beta \approx 0.05$. The deceleration timescales in Equations (A1)–(A3) were estimated for $q = 0$ and $k = 0$ with $A_0 = 1$ cm^{-3}.

A.2. Synchrotron Emission

During the deceleration phase, the post-shock magnetic field evolves as $B' \propto t^{-\frac{2(2+q)+k(1-q+\alpha)}{2(\alpha+5-k)}}$. The Lorentz factors of the lowest-energy electrons and the higher energy electrons, which are efficiently cooled by synchrotron emission are

$$\gamma_m = \gamma_m^0\left(\frac{1+z}{1.022}\right)^{\frac{2(3-k)}{\alpha+5-k}} g(p)\,\epsilon_{e,-1} A_k^{-\frac{2}{\alpha+5-k}}$$
$$\times \tilde{E}_{51}^{\frac{2}{\alpha+5-k}} t_7^{\frac{2(k-(q+2))}{\alpha+5-k}} \quad (A4)$$

Table 2
Quantities Associated with the Synchrotron Afterglow Model with Energy Injection

	$k = 0$	$k = 1.0$	$k = 1.5$	$k = 2.0$	$k = 2.5$
A_k	1 cm^{-3}	1.5×10^{19} cm^{-2}	2.7×10^{28} cm$^{-\frac{3}{2}}$	3×10^{36} cm^{-1}	1.3×10^{45} cm$^{-\frac{1}{2}}$
γ_m^0	1.9×10^3	1.2×10^3	1.0×10^3	2.1×10^3	2.5×10^3
$\gamma_c^0 (\times 10^3)$	7.2	1.3	0.8	6.4	1.3×10
$\nu_{a,1}^0$ (Hz)	1.5×10^8	1.2×10^9	2.2×10^9	2.0×10^8	1.2×10^8
$\nu_{a,2}^0$ (Hz)	6.6×10^9	1.8×10^{10}	2.5×10^{10}	8.8×10^9	6.9×10^9
$\nu_{a,3}^0$ (Hz)	8.2×10^7	1.1×10^9	2.5×10^9	1.2×10^8	6.0×10^7
ν_m^0 (Hz)	3.2×10^{11}	2.9×10^{11}	2.9×10^{11}	4.2×10^{11}	4.3×10^{11}
ν_c^0 (Hz)	9.8×10^{12}	3.9×10^{11}	1.5×10^{11}	7.3×10^{12}	2.8×10^{13}
$F_{\nu,max}^0$ (mJy)	8.3×10^5	4.2×10^6	5.5×10^6	2.3×10^5	5.0×10^4

$$\gamma_c = \gamma_c^0 \left(\frac{1+z}{1.022}\right)^{-\frac{k+1+\alpha(k-1)}{\alpha+5-k}} (1+Y)^{-1} \epsilon_{B,-2}^{-1} A_k^{-\frac{\alpha+3}{\alpha+5-k}}$$
$$\times \tilde{E}_{51}^{\frac{k-2}{\alpha+5-k}} t_7^{\frac{-1+2q-k(-2+q-\alpha)-\alpha}{\alpha+5-k}}.$$

The corresponding synchrotron break frequencies are given by

$$\nu_m = \nu_m^0 \left(\frac{1+z}{1.022}\right)^{\frac{20+k(\alpha-6)-2\alpha}{2(\alpha+5-k)}} g(p)^2 \epsilon_{e,-1}^2 \epsilon_{B,-2}^{\frac{1}{2}} A_k^{\frac{\alpha-5}{2(\alpha+5-k)}}$$
$$\times \tilde{E}_{51}^{\frac{10-k}{2(\alpha+5-k)}} t_7^{-\frac{10(2+q)+k(-7-q+\alpha)}{2(\alpha+5-k)}}$$
$$\nu_c = \nu_c^0 \left(\frac{1+z}{1.022}\right)^{-\frac{8-2\alpha+k(3\alpha+2)}{2(\alpha+5-k)}} \epsilon_{B,-2}^{-\frac{3}{2}}$$
$$\times (1+Y)^{-2} A_k^{-\frac{3(\alpha+3)}{2(\alpha+5-k)}} \tilde{E}_{51}^{\frac{3(k-2)}{2(\alpha+5-k)}} t_7^{-\frac{8-6q+k(-7+3q-3\alpha)+4\alpha}{2(\alpha+5-k)}}. \quad \text{(A5)}$$

In the self-absorption regime, the synchrotron break frequencies are

$$\nu_{a,1} = \nu_{a,1}^0 \left(\frac{1+z}{1.022}\right)^{-\frac{55+8\alpha-k(21+4\alpha)}{5(\alpha+5-k)}} g(p)^{-1}$$
$$\epsilon_{e,-1}^{-1} \epsilon_{B,-2}^{\frac{1}{5}}$$
$$\times A_k^{\frac{25+4\alpha}{5(\alpha+5-k)}} \tilde{E}_{51}^{-\frac{4k+5}{5(\alpha+5-k)}} t_6^{\frac{25+5q+4k(-5-q-\alpha)+3\alpha}{5(\alpha+5-k)}}$$
$$\nu_{a,2} = \nu_{a,2}^0 \left(\frac{1+z}{1.022}\right)^{\frac{-2p(-10+\alpha)+kp(-6+\alpha)+6k(4+\alpha)-12(5+\alpha)}{2(p+4)(\alpha+5-k)}}$$
$$\times g(p)^{\frac{2(p-1)}{p+4}} \epsilon_{e,-1}^{\frac{2(p-1)}{p+4}} A_k^{\frac{p(\alpha-5)+6(\alpha+5)}{2(p+4)(\alpha+5-k)}} \epsilon_{B,-2}^{\frac{p+2}{2(p+4)}} \tilde{E}_{51}^{\frac{10p-k(p+6)}{2(p+4)(\alpha+5-k)}}$$
$$\times t_6^{-\frac{10p(2+q)-4(5+\alpha)+k(22-6q+6\alpha+p(-7-q+\alpha))}{2(p+4)(\alpha+5-k)}},$$
$$\nu_{a,3} = \nu_{a,3}^0 \left(\frac{1+z}{1.022}\right)^{-\frac{20+13\alpha-k(16+9\alpha)}{5(\alpha+5-k)} \times 5(\alpha+5-k)} (1+Y)$$
$$\times \epsilon_{B,-2}^{\frac{6}{5}} A_k^{\frac{3(3\alpha+10)}{5(\alpha+5-k)}} \tilde{E}_{51}^{\frac{15-9k}{5(\alpha+5-k)}} t_6^{\frac{10-15q+k(-20+9q-9\alpha)+8\alpha}{5(\alpha+5-k)}}. \quad \text{(A6)}$$

The spectral peak flux density becomes

$$F_{\nu,max}^{syn} = F_{\nu,max}^{syn,0} \left(\frac{1+z}{1.022}\right)^{\frac{4(1-\alpha)+k(2+3\alpha)}{2(\alpha+5-k)}}$$
$$\times \epsilon_{B,-2}^{\frac{1}{2}} d_{z,26.5}^{-2} A_k^{\frac{3\alpha+7}{2(\alpha+5-k)}} \tilde{E}_{51}^{\frac{8-3k}{2(\alpha+5-k)}} t_7^{\frac{14-8q+k(-7+3q-3\alpha)+6\alpha}{2(\alpha+5-k)}}. \quad \text{(A7)}$$

The quantities γ_m^0, γ_c^0, ν_m^0, ν_c^0, and $F_{\nu,max}^0$ given in Equations (A4)–(A7) are reported in Table 2 for $k = 0$, 1, 1.5, 2, and 2.5.

Using the synchrotron break frequencies (Equation (A5)) and the spectral peak flux density (Equation (A7)), the synchrotron light curve for $\nu_{a,3} \leqslant \nu_c \leqslant \nu_m$ is

$$F_\nu^{syn} \propto \begin{cases} t^{\frac{5+\alpha+k(2-q+\alpha)}{\alpha+5-k}} \nu^2, & \nu < \nu_{a,3}, \\ t^{\frac{25-15q+2k(-7+3q-3\alpha)+11\alpha}{3(\alpha+5-k)}} \nu^{\frac{1}{3}}, & \nu_{a,3} < \nu < \nu_c, \\ t^{\frac{20-10q+k(-7+3q-3\alpha)+8\alpha}{4(\alpha+5-k)}} \nu^{-\frac{1}{2}}, & \nu_c < \nu < \nu_m, \\ t^{-\frac{10p(2+q)-8(5+\alpha)+kp(-7-q+\alpha)+2k(7-q+\alpha)}{4(\alpha+5-k)}} \nu^{-\frac{p}{2}}, & \nu_m < \nu, \end{cases} \quad \text{(A8)}$$

for $\nu_{a,1} \leqslant \nu_m \leqslant \nu_c$ is

$$F_\nu^{syn} \propto \begin{cases} t^{\frac{2(1+k-2q+\alpha)}{\alpha+5-k}} \nu^2, & \nu < \nu_{a,1}, \\ t^{\frac{31-7q+2k(-7+2q-2\alpha)+9\alpha}{3(\alpha+5-k)}} \nu^{\frac{1}{3}}, & \nu_{a,1} < \nu < \nu_m, \\ t^{-\frac{10p(2+q)+6(-8+q-2\alpha)+k(21-5q+5\alpha+p(-7-q+\alpha))}{4(\alpha+5-k)}} \nu^{\frac{p-1}{2}} \not{\nu_m} \lessgtr \nu_c, \\ t^{-\frac{10p(2+q)-8(5+\alpha)+kp(-7-q+\alpha)+2k(7-q+\alpha)}{4(\alpha+5-k)}} \nu^{-\frac{p}{2}} \nu_c < \nu, \end{cases} \quad \text{(A9)}$$

and for $\nu_m \leqslant \nu_{a,2} \leqslant \nu_c$ is

$$F_\nu^{syn} \propto \begin{cases} t^{\frac{2(1+k-2q+\alpha)}{\alpha+5-k}} \nu^2, & \nu < \nu_m, \\ t^{\frac{28+k-6q-kq+8\alpha+k\alpha}{4(\alpha+5-k)}} \nu^{\frac{5}{2}}, & \nu_m < \nu < \nu_{a,2}, \\ t^{-\frac{10p(2+q)+6(-8+q-2\alpha)+k(21-5q+5\alpha+p(-7-q+\alpha))}{4(\alpha+5-k)}} \nu^{\frac{p-1}{2}} \nu_{a,2} < \nu \lessgtr \nu_c, \\ t^{-\frac{10p(2+q)-8(5+\alpha)+kp(-7-q+\alpha)+2k(7-q+\alpha)}{4(\alpha+5-k)}} \nu^{-\frac{p}{2}} \nu_c < \nu, \end{cases} \quad \text{(A10)}$$

respectively.

Quantities: $\tilde{E} = 10^{49}$ erg, $d_z \approx 100$ Mpc ($z = 0.022$), $p = 2.6$, $\epsilon_B = 10^{-3}$, $\epsilon_e = 10^{-1}$, $\alpha = 3.0$, $q = 0.7$, $t = 10^7$ s.

ORCID iDs

N. Fraija ⓘ https://orcid.org/0000-0002-0173-6453
B. Betancourt Kamenetskaia ⓘ https://orcid.org/0000-0002-2516-5739
A. Galvan-Gamez ⓘ https://orcid.org/0000-0001-5193-3693
M. G. Dainotti ⓘ https://orcid.org/0000-0003-4442-8546
R. L. Becerra ⓘ https://orcid.org/0000-0002-0216-3415
S. Dichiara ⓘ https://orcid.org/0000-0001-6849-1270
P. Veres ⓘ https://orcid.org/0000-0002-2149-9846

References

Abbott, B. P., Abbott, R., Abbott, T. D., et al. 2017a, PhRvL, 119, 161101
Abbott, B. P., Abbott, R., Abbott, T. D., et al. 2017b, ApJL, 848, L12
Abbott, B. P., Abbott, R., Abbott, T. D., et al. 2017c, ApJL, 848, L12
Acciari, V. A., Ansoldi, S., Antonelli, L. A., et al. 2021, ApJ, 908, 90
Alexander, K. D., Margutti, R., Blanchard, P. K., et al. 2018, ApJL, 863, L18
Ando, S., & Beacom, J. F. 2005, PhRvL, 95, 061103
Arcavi, I., Hosseinzadeh, G., Howell, D. A., et al. 2017, Natur, 551, 64
Barnes, J., & Kasen, D. 2013, ApJ, 775, 18
Barniol Duran, R., & Giannios, D. 2015, MNRAS, 454, 1711
Barthelmy, S. D., Cannizzo, J. K., Gehrels, N., et al. 2005, ApJL, 635, L133
Barthelmy, S. D., Baumgartner, W. H., Cummings, J. R., et al. 2013, GCN, 14741, 1
Bauswein, A., Goriely, S., & Janka, H. T. 2013, ApJ, 773, 78
Becerra, R. L., Watson, A. M., Fraija, N., et al. 2019a, ApJ, 872, 118
Becerra, R. L., De Colle, F., Watson, A. M., et al. 2019b, ApJ, 887, 254
Beniamini, P., Granot, J., & Gill, R. 2020, MNRAS, 493, 3521
Berger, E. 2014, ARA&A, 52, 43
Berger, E., Fong, W., & Chornock, R. 2013, ApJL, 774, L23
Blandford, R. D., & McKee, C. F. 1976, PhFl, 19, 1130
Blandford, R. D., & Znajek, R. L. 1977, MNRAS, 179, 433
Bloom, J. S., Kulkarni, S. R., Djorgovski, S. G., et al. 1999, Natur, 401, 453
Bromberg, O., Nakar, E., & Piran, T. 2011, ApJL, 739, L55
Buccianti, N., Quataert, E., Arons, J., Metzger, B. D., & Thompson, T. A. 2007, MNRAS, 380, 1541
Burrows, D. N., Romano, P., Falcone, A., et al. 2005, Sci, 309, 1833
Cantiello, M., Jensen, J. B., Blakeslee, J. P., et al. 2018, ApJL, 854, L31
Chevalier, R. A. 1989, ApJ, 346, 847
Chevalier, R. A., & Fransson, C. 2006, ApJ, 651, 381
Chincarini, G., Moretti, A., Romano, P., et al. 2007, ApJ, 671, 1903
Connaughton, V., , GBM-LIGO Group, Blackburn, L., et al. 2017, GCN Circ., 21506, 1
Coulter, D. A., Foley, R. J., Kilpatrick, C. D., et al. 2017, Sci, 358, 1556
Cowperthwaite, P. S., Berger, E., Villar, V. A., et al. 2017, ApJL, 848, L17
Dai, Z. G., & Lu, T. 1998, A&A, 333, L87
Dai, Z. G., & Lu, T. 1999, ApJL, 519, L155
Dai, Z. G., & Lu, T. 2000, ApJ, 537, 803
Dai, Z. G., Wang, X. Y., Wu, X. F., & Zhang, B. 2006, Sci, 311, 1127
Dall'Osso, S., Perna, R., Tanaka, T. L., & Margutti, R. 2017, MNRAS, 464, 4399
D'Avanzo, P., Campana, S., Salafia, O. S., et al. 2018a, A&A, 613, L1
D'Avanzo, P., Campana, S., Salafia, O. S., et al. 2018b, A&A, 613, L1
Davies, M. B., Benz, W., Piran, T., & Thielemann, F. K. 1994, ApJ, 431, 742
Dessart, L., Ott, C. D., Burrows, A., Rosswog, S., & Livne, E. 2009, ApJ, 690, 1681
Dhawan, S., Bulla, M., Goobar, A., Sagués Carracedo, A., & Setzer, C. N. 2020, ApJ, 888, 67
Duncan, R. C., & Thompson, C. 1992, ApJL, 392, L9
Fan, Y., & Piran, T. 2006, MNRAS, 369, 197
Fernández, R., Kasen, D., Metzger, B. D., & Quataert, E. 2015, MNRAS, 446, 750
Fong, W., Blanchard, P. K., Alexander, K. D., et al. 2019, ApJL, 883, L1
Fox, D. B., Frail, D. A., Price, P. A., et al. 2005, Natur, 437, 845
Fraija, N. 2014, MNRAS, 437, 2187
Fraija, N., De Colle, F., Veres, P., et al. 2019a, ApJ, 871, 123
Fraija, N., Kamenetskaia, B. B., Dainotti, M. G., et al. 2021a, ApJ, 907, 78
Fraija, N., Laskar, T., Dichiara, S., et al. 2020, ApJ, 905, 112
Fraija, N., Lopez-Camara, D., Pedreira, A. C. C. D. E. S., et al. 2019b, ApJ, 884, 71
Fraija, N., Pedreira, A. C. C. D. E. S., & Veres, P. 2019c, ApJ, 871, 200
Fraija, N., Veres, P., Beniamini, P., et al. 2021b, ApJ, 918, 12
Gal-Yam, A. 2017, Observational and Physical Classification of Supernovae (New York: Springer International), 1
Galama, T. J., Vreeswijk, P. M., van Paradijs, J., et al. 1998, Natur, 395, 670
Gehrels, N., Norris, J. P., Barthelmy, S. D., et al. 2006, Natur, 444, 1044
Goldstein, A., Veres, P., Burns, E., et al. 2017, ApJL, 848, L14
Goriely, S., Bauswein, A., & Janka, H.-T. 2011, ApJL, 738, L32
Gottlieb, O., Nakar, E., & Piran, T. 2018a, MNRAS, 473, 576
Gottlieb, O., Nakar, E., Piran, T., & Hotokezaka, K. 2018b, MNRAS, 479, 588
Grossman, D., Korobkin, O., Rosswog, S., & Piran, T. 2014, MNRAS, 439, 757
Hajela, A., Margutti, R., Alexander, K. D., et al. 2019, ApJL, 886, L17
Hajela, A., Margutti, R., Bright, J. S., et al. 2022, ApJ, 927, L17
Hascoët, R., Beloborodov, A. M., Daigne, F., & Mochkovitch, R. 2017, MNRAS, 472, L94

Hjorth, J., Watson, D., Fynbo, J. P. U., et al. 2005, Natur, 437, 859
Hotokezaka, K., Kiuchi, K., Shibata, M., Nakar, E., & Piran, T. 2018, ApJ, 867, 95
Hotokezaka, K., Kyutoku, K., Tanaka, M., et al. 2013, ApJL, 778, L16
Hotokezaka, K., & Piran, T. 2015, MNRAS, 450, 1430
Huang, Y. F., & Cheng, K. S. 2003, MNRAS, 341, 263
Huang, Y. F., Dai, Z. G., & Lu, T. 1998, A&A, 336, L69
Huang, Y. F., Dai, Z. G., & Lu, T. 1999, MNRAS, 309, 513
Ioka, K., Toma, K., Yamazaki, R., & Nakamura, T. 2006, A&A, 458, 7
Izzo, L., Auchettl, K., Hjorth, J., et al. 2020, A&A, 639, L11
Izzo, L., de Ugarte Postigo, A., Maeda, K., et al. 2019, Natur, 565, 324
Janiuk, A., Perna, R., Di Matteo, T., & Czerny, B. 2004, MNRAS, 355, 950
Jin, Z.-P., Hotokezaka, K., Li, X., et al. 2016, NatCo, 7, 12898
Jin, Z. P., Yan, T., Fan, Y. Z., & Wei, D. M. 2007, ApJL, 656, L57
Kasen, D., Badnell, N. R., & Barnes, J. 2013, ApJ, 774, 25
Kasen, D., Fernández, R., & Metzger, B. D. 2015, MNRAS, 450, 1777
Kasliwal, M. M., Korobkin, O., Lau, R. M., Wollaeger, R., & Fryer, C. L. 2017a, ApJL, 843, L34
Kasliwal, M. M., Nakar, E., Singer, L. P., et al. 2017b, Sci, 358, 1559
Kathirgamaraju, A., Barniol Duran, R., & Giannios, D. 2016, MNRAS, 461, 1568
Kathirgamaraju, A., Giannios, D., & Beniamini, P. 2019, MNRAS, 487, 3914
Kisaka, S., Ioka, K., Kashiyama, K., & Nakamura, T. 2018, ApJ, 867, 39
Kiuchi, K., Kyutoku, K., Sekiguchi, Y., Shibata, M., & Wada, T. 2014, PhRvD, 90, 041502
Kouveliotou, C., Meegan, C. A., Fishman, G. J., et al. 1993, ApJL, 413, L101
Kulkarni, S. R., Frail, D. A., Wieringa, M. H., et al. 1998, Natur, 395, 663
Kumar, P., Narayan, R., & Johnson, J. L. 2008a, Sci, 321, 376
Kumar, P., Narayan, R., & Johnson, J. L. 2008b, MNRAS, 388, 1729
Kumar, P., & Piran, T. 2000, ApJ, 532, 286
Kyutoku, K., Ioka, K., & Shibata, M. 2014, MNRAS, 437, L6
Lamb, G. P., & Kobayashi, S. 2017, MNRAS, 472, 4953
Lamb, G. P., & Kobayashi, S. 2018, MNRAS, 478, 733
Lamb, G. P., Tanvir, N. R., Levan, A. J., et al. 2019, ApJ, 883, 48
Laskar, T., Alexander, K. D., Berger, E., et al. 2018, ApJ, 862, 94
Laskar, T., Berger, E., Margutti, R., et al. 2015, ApJ, 814, 1
Lattimer, J. M., & Schutz, B. F. 2005, ApJ, 629, 979
Lazzati, D., López-Cámara, D., Cantiello, M., et al. 2017, ApJL, 848, L6
Lazzati, D., Perna, R., Morsony, B. J., et al. 2018, PhRvL, 120, 241103
Lee, H. K., Wijers, R. A. M. J., & Brown, G. E. 2000, PhR, 325, 83
Lei, W.-H., Zhang, B., & Liang, E.-W. 2013, ApJ, 765, 125
Li, L.-X., & Paczyński, B. 1998, ApJL, 507, L59
Liang, E.-W., Li, L., Gao, H., et al. 2013, ApJ, 774, 13
Livio, M., & Waxman, E. 2000, ApJ, 538, 187
Lyman, J. D., Lamb, G. P., Levan, A. J., et al. 2018, NatAs, 2, 751
MacFadyen, A. I., & Woosley, S. E. 1999, ApJ, 524, 262
MacFadyen, A. I., Woosley, S. E., & Heger, A. 2001, ApJ, 550, 410
Margalit, B., & Piran, T. 2020, MNRAS, 495, 4981
Margutti, R., Alexander, K. D., Xie, X., et al. 2018, ApJL, 856, L18
Margutti, R., Berger, E., Fong, W., et al. 2017a, ApJL, 848, L20
Margutti, R., Kamble, A., Milisavljevic, D., et al. 2017b, ApJ, 835, 140
Margutti, R., Milisavljevic, D., Soderberg, A. M., et al. 2014, ApJ, 797, 107
Mészáros, P., & Waxman, E. 2001, PhRvL, 87, 171102
Metzger, B. D. 2017, LRR, 20, 3
Metzger, B. D. 2019, LRR, 23, 1
Metzger, B. D., Bauswein, A., Goriely, S., & Kasen, D. 2015, MNRAS, 446, 1115
Metzger, B. D., Beniamini, P., & Giannios, D. 2018, ApJ, 857, 95
Metzger, B. D., & Berger, E. 2012, ApJ, 746, 48
Metzger, B. D., & Fernández, R. 2014, MNRAS, 441, 3444
Metzger, B. D., Giannios, D., Thompson, T. A., Bucciantini, N., & Quataert, E. 2011, MNRAS, 413, 2031
Metzger, B. D., Martínez-Pinedo, G., Darbha, S., et al. 2010, MNRAS, 406, 2650
Miller, J. M., Ryan, B. R., Dolence, J. C., et al. 2019, PhRvD, 100, 023008
Modjaz, M., Bianco, F. B., Siwek, M., et al. 2020, ApJ, 892, 153
Mooley, K. P., Deller, A. T., Gottlieb, O., et al. 2018, Natur, 561, 355
Murguia-Berthier, A., Montes, G., Ramirez-Ruiz, E., De Colle, F., & Lee, W. H. 2014, ApJL, 788, L8
Nagakura, H., Hotokezaka, K., Sekiguchi, Y., Shibata, M., & Ioka, K. 2014, ApJL, 784, L28
Nakar, E., & Piran, T. 2017, ApJ, 834, 28
Nicholl, M., Berger, E., Kasen, D., et al. 2017, ApJL, 848, L18
Nicholl, M., Blanchard, P. K., Berger, E., et al. 2020, NatAs, 4, 893
Nousek, J. A., Kouveliotou, C., Grupe, D., et al. 2006, ApJ, 642, 389

Paczyński, B. 1998, ApJL, 494, L45
Perego, A., Rosswog, S., Cabezón, R. M., et al. 2014, MNRAS, 443, 3134
Pereyra, M., Fraija, N., Watson, A. M., et al. 2022, MNRAS, 511, 6205
Perna, R., Armitage, P. J., & Zhang, B. 2006, ApJL, 636, L29
Piran, T., Nakar, E., & Rosswog, S. 2013, MNRAS, 430, 2121
Piro, A. L., & Ott, C. D. 2011, ApJ, 736, 108
Planck Collaboration, Ade, P. A. R., Aghanim, N., et al. 2016, A&A, 594, A13
Popham, R., Woosley, S. E., & Fryer, C. 1999, ApJ, 518, 356
Price, D. J., & Rosswog, S. 2006, Sci, 312, 719
Proga, D., & Zhang, B. 2006, MNRAS, 370, L61
Quataert, E., & Kasen, D. 2012, MNRAS, 419, L1
Rees, M. J., & Mészáros, P. 1998, ApJL, 496, L1
Resmi, L., Schulze, S., Ishwara-Chandra, C. H., et al. 2018, ApJ, 867, 57
Rosswog, S. 2005, ApJ, 634, 1202
Rosswog, S. 2007, MNRAS, 376, L48
Rosswog, S., Liebendörfer, M., Thielemann, F. K., et al. 1999, A&A, 341, 499
Ruffert, M., Janka, H. T., Takahashi, K., & Schaefer, G. 1997, A&A, 319, 122
Sari, R., & Mészáros, P. 2000, ApJL, 535, L33
Sari, R., Piran, T., & Narayan, R. 1998, ApJL, 497, L17
Savchenko, V., Ferrigno, C., Kuulkers, E., et al. 2017, ApJL, 848, L15
Shibata, M., & Hotokezaka, K. 2019, ARNPS, 69, 41
Shibata, M., & Taniguchi, K. 2006, PhRvD, 73, 064027
Siegel, D. M., Ciolfi, R., Harte, A. I., & Rezzolla, L. 2013, PhRvD, 87, 121302
Siegel, D. M., & Metzger, B. D. 2017, PhRvL, 119, 231102
Sironi, L., & Giannios, D. 2013, ApJ, 778, 107
Smartt, S. J., Chen, T. W., Jerkstrand, A., et al. 2017, Natur, 551, 75
Soares-Santos, M., Holz, D. E., Annis, J., et al. 2017, ApJL, 848, L16
Sobacchi, E., Granot, J., Bromberg, O., & Sormani, M. C. 2017, MNRAS, 472, 616
Tan, J. C., Matzner, C. D., & McKee, C. F. 2001, ApJ, 551, 946
Tanaka, M., & Hotokezaka, K. 2013, ApJ, 775, 113
Tanvir, N. R., Levan, A. J., Fruchter, A. S., et al. 2013, Natur, 500, 547
Tanvir, N. R., Levan, A. J., González-Fernández, C., et al. 2017, ApJL, 848, L27
Tchekhovskoy, A., McKinney, J. C., & Narayan, R. 2008, MNRAS, 388, 551
Thompson, C. 1994, MNRAS, 270, 480
Thompson, T. A., Chang, P., & Quataert, E. 2004, ApJ, 611, 380
Toma, K., Ioka, K., Yamazaki, R., & Nakamura, T. 2006, ApJL, 640, L139
Totani, T. 2003, ApJ, 598, 1151
Troja, E., Castro-Tirado, A. J., Becerra González, J., et al. 2019, MNRAS, 489, 2104
Troja, E., Piro, L., van Eerten, H., et al. 2017, Natur, 551, 71
Troja, E., van Eerten, H., Zhang, B., et al. 2020, MNRAS, 498, 5643
Urrutia, G., De Colle, F., Murguia-Berthier, A., & Ramirez-Ruiz, E. 2021, MNRAS, 503, 4363
Usov, V. V. 1992, Natur, 357, 472
Valenti, S., Benetti, S., Cappellaro, E., et al. 2008, MNRAS, 383, 1485
van der Horst, A. J., Kamble, A., Wijers, R. A. M. J., et al. 2007, RSPTA, 365, 1241
van der Horst, A. J., Paragi, Z., de Bruyn, A. G., et al. 2014, MNRAS, 444, 3151
Vaughan, S., Goad, M. R., Beardmore, A. P., et al. 2006, ApJ, 638, 920
Villasenor, J. S., Lamb, D. Q., Ricker, G. R., et al. 2005, Natur, 437, 855
Wanajo, S., Sekiguchi, Y., Nishimura, N., et al. 2014, ApJL, 789, L39
Wheeler, J. C., Yi, I., Höflich, P., & Wang, L. 2000, ApJ, 537, 810
Wijers, R. A. M. J., Rees, M. J., & Meszaros, P. 1997, MNRAS, 288, L51
Woosley, S. E. 1993, ApJ, 405, 273
Woosley, S. E., & Bloom, J. S. 2006a, ARA&A, 44, 507
Woosley, S. E., & Bloom, J. S. 2006b, ARA&A, 44, 507
Woosley, S. E., & Heger, A. 2012, ApJ, 752, 32
Wu, X.-F., Hou, S.-J., & Lei, W.-H. 2013, ApJL, 767, L36
Xiao, D., & Dai, Z.-G. 2019, ApJ, 878, 62
Yang, B., Jin, Z.-P., Li, X., et al. 2015, NatCo, 6, 7323
Yi, S.-X., Wu, X.-F., & Dai, Z.-G. 2013, ApJ, 776, 120
Zhang, B., Fan, Y. Z., Dyks, J., et al. 2006, ApJ, 642, 354
Zhang, B., & Mészáros, P. 2001, ApJL, 552, L35
Zhang, B., & Mészáros, P. 2002, ApJ, 566, 712
Zhang, W., Woosley, S. E., & Heger, A. 2008, ApJ, 679, 639
Zhao, L., Gao, H., Lei, W., Lan, L., & Liu, L. 2021, ApJ, 906, 60